Kaunas University of Technology

Faculty of Mathematic and Natural Sciences

Synthesis and Characterization of Titanium Doped Diamond-like Carbon Coatings

Master's Final Degree Project

Hassan Zhairabany

Project author

Prof. dr. Liutauras Marcinauskas

Supervisor

Kaunas, 2021

Kaunas University of Technology

Faculty of Mathematic and Natural Sciences

Synthesis and Characterization of Titanium Doped Diamond-like Carbon Coatings

Master's Final Degree Project

Materials Science 6211FX009

Hassan Zhairabany

Project author

Prof. dr. Liutauras Marcinauskas

Supervisor

Prof. dr. Tomas TAMULEVIČIUS

Reviewer

Kaunas, 2021

Kaunas University of Technology

Faculty of Mathematic and Natural Sciences

Hassan Zhairabany

Synthesis and Characterization of Titanium Doped Diamond-like Carbon Coatings

Declaration of Academic Integrity

I confirm the following:

1. I have prepared the final degree project independently and honestly without any violations of the copyrights or other rights of others, following the provisions of the Law on Copyrights and Related Rights of the Republic of Lithuania, the Regulations on the Management and Transfer of Intellectual Property of Kaunas University of Technology (hereinafter – University) and the ethical requirements stipulated by the Code of Academic Ethics of the University;
2. All the data and research results provided in the final degree project are correct and obtained legally; none of the parts of this project are plagiarised from any printed or electronic sources; all the quotations and references provided in the text of the final degree project are indicated in the list of references;
3. I have not paid anyone any monetary funds for the final degree project or the parts thereof unless required by the law;
4. I understand that in the case of any discovery of the fact of dishonesty or violation of any rights of others, the academic penalties will be imposed on me under the procedure applied at the University; I will be expelled from the University and my final degree project can be submitted to the Office of the Ombudsperson for Academic Ethics and Procedures in the examination of a possible violation of academic ethics.

Hassan Zhairabany

Confirmed electronically

Zhairabany, Hassan. Synthesis and Characterization of Titanium Doped Diamond-like Carbon Coatings Master's Final Degree Project /supervisor / Prof. Liutauras Marcinauskas; Faculty of Mathematic and Natural Sciences, Kaunas Univesity of Technology.

Study field and area (study field group): Technology sciences (F), Technology of materials (F03).

Keywords: diamond-like carbon films, titanium, atomic force microscopy, surface morphology, friction force.

Kaunas, 2021. 58 p.

Summary

In this work, the doped diamond-like carbon (DLC) films were deposited on Si (100) substrates by magnetron sputtering, where graphite and Ti targets were used. The Ti cathode current was changed from 0 A to 1.00 A. The target-substrate distance was fixed at 3 cm, the argon pressure in the deposition chamber was between 2-3 Pa, and the deposition duration was ~600 s.

The surface morphology, adhesion, and friction of titanium doped diamond-like carbon films were investigated using Atomic Force Microscopy (AFM). Then the data were extracted and analyzed using Gwyddion software. The elemental composition of the films was also investigated using the energy dispersive X-Ray spectroscopy (EDS). Eventually, the structure of the films was investigated using Raman Spectroscopy (RS). Meanwhile, the light transmittance was measured using the IR-visible-UV spectrophotometer.

The root mean square roughness values were slightly increased from ~1.2 to ~2.1 nm, and the Skewness and Kurtosis were decreased with the increase of Ti concentration. The results indicated that the surfaces of the films were self-affine shape. The increase of the Ti content in the DLC films resulted in a higher fraction of sp^2 carbon sites and graphitization. The average adhesion values were decreased from ~14 to ~6 nN with an enhancement of Ti amount in the films. The friction forces measured using the sharp cantilever fluctuated (topography contribution). The DLC film with the lowest Ti concentration showed the lowest friction force value of ~14 nN at 80 nN normal force (friction coefficient μ ~0.175). The lateral deflection values measured using the “PMMA” cantilever, with the diameter of probe equals 1.5 μm, show much stability with the normal force variation between 20 and 100 nN. The lowest lateral deflection signal was obtained for the DLC film with ~23 at. % Ti.

Zhairabany, Hassan. Titanu legiruotų deimanto tipo anglies dangų formavimas ir tyrimas Magistro baigiamojo laipsnio projektas / vadovas /Prof. Liutauras Marcinauskas; Kauno technologijos universitetas; Matematikos ir gamtos mokslų fakultetas

Studijų kryptis ir sritis (studijų krypčių grupė): Technologijos mokslai (F), Medžiagų technologija (F03)

Reikšminiai žodžiai: deimanto tipo anglies dangos, titanas, atominių jėgų mikroskopija, paviršiaus morfologija, trinties jėga.

Kaunas, 2021. 58 p.

Santrauka

Šiame darbe legiruotos deimanto tipo dangos (DTA) buvo suformuotos ant silicio (100) pagrindo plokštelių naudojant magnetroninį dulkinimą. Dangų formavimui naudoti grafito ir titano taikiniai, keičiant titano katodo srovę nuo 0 A iki 1,00 A. Dangos formuotos naudojant argono dujas (slėgis 2-3 Pa), esant 3 cm atstumui nuo katodų, o formavimo trukmė buvo 600 s.

Titanu legiruotų deimanto tipo anglies dangų paviršiaus morfologija, adhezija ir trintis buvo tiriama naudojant atominių jėgų mikroskopiją (AFM), o gauti rezultatai analizuoti naudojant "Gwyddion" programinį paketą. Suformuotų dangų elementinė sudėtis tirta rentgeno spindulių energijos dispersijos spektroskopija. Dangų struktūros tyrimui naudota Ramano sklaidos spektroskopija, o pralaidumas matuotas UV-Vis spektrometru.

AFM tyrimai parodė, kad dangų vidutinis kvadratinis šiurkštis padidėjo nuo ~1,2 nm iki ~2,1 nm, asimetrijos koeficiento ir eksceso vertės sumažėja didėjant titano koncentracijai dangos. Atlikti tyrimai rodė, kad dangos pasižymi tolygiai atsikartojančiu paviršiumi. Didėjant titano koncentracijai DTA dangose, daugėja sp^2 C=C ryšių kiekis ir vyksta dangų grafitizacija, kas lemia paviršiaus adhezijos jėgos sumažėjimą nuo ~14 nN iki ~6 nN. Suformuotų legiruotų DTA dangų trinties jėgos ir koeficientų vertės priklauso nuo matavimams naudoto atominių jėgų mikroskopo antgalio (zondo) formos. Matavimams naudojant smailų antgalį gaunamas didelis rezultatų išsibarstymas, o mažiausia trintis jėga ~14 nN (trinties koeficientas ~0,175) yra gaunama su apkrovos jėga lygia 80 nN, dangai turinčiai mažiausią Ti kiekį. Matavimams naudojant sferinės formos (skersmuo 1,5 µm) polimerinį antgalį ir apkrovos jėgą keičiant nuo 20 nN iki 100 nN, mažiausios atsako vertės gaunamos titanu legiruotoje DTA dangoje, kurioje Ti koncentracija buvo ~23 %.

Table of contents

List of figures **7**
List of tables **9**
List of abbreviations **10**
Introduction **11**
1. Magnetron Sputtering Deposition Technique **12**
1.1. Fundamental & concept of Sputtering process 12
1.2. The concept of Magnetron Sputtering and its configurations 13
1.3. Technical description and some key features 15
2. Diamond like Carbon Thin Films **17**
2.1. Classification of DLC films and their types 17
2.2. Raman spectroscopy for characterization of DLC films 19
2.3. Applications and utilizations 21
2.4. Titanium doped diamond-like carbon films 22
3. Experimental and methods **28**
3.1. Deposition of the doped DLC films 28
3.2. Atomic Force Microscopy 29
3.2.1. Roughness 32
3.2.2. Fractal dimension and self-affinity 32
3.2.3. Adhesion 35
3.2.4. Friction measurements 35
3.3. Raman Spectroscopy measurements 37
3.4. IR-visible-UV spectrophotometer 37
3.5. Energy Dispersive X-Ray Spectroscopy 38
4. Results and discussion **39**
4.1. Surfaces morphology (AFM) 39
4.2. Light transmittance 42
4.3. Raman spectra 43
4.4. Adhesion (AFM) 45
4.5. Friction using “ContAl-G” cantilever (AFM) 47
4.6. Friction using “PMMA-1.5” cantilever (AFM) 48
Conclusions **50**
List of references **52**
Appendices **57**
Appendix 1. JPK software 57
Appendix 2. Gwyddion software 58

List of figures

Fig. 1. The sputtering process schematic [17] 12
Fig. 2. Illustration of the Magnetron Sputtering Deposition [17]. 14
Fig. 3. Unbalanced Magnetron Sputtering configuration [24]. 15
Fig. 4. The principal components of a magnetron sputtering deposition device [17]. 16
Fig. 5. (a) sp^1 (b) sp^2; (c) sp^3; carbon bonding configuration [41]. 17
Fig. 6. From the right, the graphite and the diamond structure of carbon atoms respectively [43]. . 17
Fig. 7. The variation of the and the elastic modulus and the hardness with the concentration of three different dopant metals in the DLC thin films, deposited by FCVAE [58] 18
Fig. 8. A typical spectra of scattered light in optical fiber [57]. 19
Fig. 9. The carbon atoms' vibration mode. From the right, the breathing A_{1g} mode represents the D-peak, the stretching E_{2g} mode stands for the G-peak [59]. 19
Fig. 10. On the left, the amorphization trajectory, shows the G position variation as well the peaks intensity ratio with 514.5 nm excitation versus the sp^3 amount. On the right, the Raman spectra of typical carbon films [44, 63] 20
Fig. 11. Automotive components with DLC deposition [9]. 21
Fig. 12. The Raman spectra of the films and their friction coefficient [27] 23
Fig. 13. The XPS and its decomposition spectra. (a) DLC film; and (b) Ti-doped DLC film. On the right, the Ti-doped DLC film TEM micrograph [28]. 24
Fig. 14. The Raman spectra of each sample and The XPS C 1s peak of the films with different Ar/CH_4 flow ratios [15]. 24
Fig. 15. The G-peak position and I_D/I_G of the films deposited at various Ar/CH_4 [15]. 25
Fig. 16. On the right, the grain size of the TiC versus the carbon concentration. On the left, the percentage of each phases as a function of total carbon concentration [39]. 25
Fig. 17. The average friction coefficient and wear rate variation at several Ar/CH_4 [15]. 26
Fig. 18. The Magnetron Sputtering deposition system photos. 28
Fig. 19. A typical AFM setup [49] & Photograph of the AFM stage in Jena Otto-Schott institute [48]. 29
Fig. 20. The operation modes and their region in the force versus distance graph [51]. 30
Fig. 21. SEM images of the three cantilevers types in the **Table 3**[29, 31, 52] 32
Fig. 22 . The height distribution graphs of different surfaces [60]. 33
Fig. 23. The surface roughness power spectrum of two different roughness surfaces [60]. 34
Fig. 24. The vertical deflection versus the height profile [51]. 35
Fig. 25. The calibration method used, by Özoğul, A.[56] 36
Fig. 26. The Raman spectroscopy photo (Renishaw in Via Spectrometer with accessories) used in National innovation and entrepreneurship center in KTU. 37
Fig. 27. Topography surface of the films. 39
Fig. 28. The root mean squared roughness R_q, skwevness and kurtosis versus the Ti target discharge current. 40
Fig. 29. The elemental atomic percentage versus the Ti target discharge current. 42
Fig. 30. The light transmittance of the samples. 43
Fig. 31. The Raman spectra of the samples between 1000 and 1800 cm^{-1} wavelength. 43
Fig. 32. The Raman spectra of each sample fitted with Gaussian function. The average spectra parameters were included in the graph of each sample. 44
Fig. 33. The Raman spectra main parameters variation versus the Ti discharge current. 45

Fig. 34. The adhesion figures of (a) DLC, (b) Ti-DLC1, (c) Ti-DLC2, (d) Ti-DLC3 films............ 46
Fig. 35. The average adhesion values of each sample.. 46
Fig. 36. The lateral deflection of the sample Ti-DLC2 at 80nN set point, from the right, trace and retrace channels. 47
Fig. 37. On the left the friction values at each normal force. And on the right the graph of the friction force versus the normal force measured using the sharp cantilever "ContAl-G". 47
Fig. 38. The lateral deflection of the sample at 25nN set point, from the right, trace and retrace channels. 48
Fig. 39. The lateral deflection signal in volt for each samples versus the normal force in nN......... 49
Fig. 40. The measurement parameters, as seen from the JPK software, of the sample Ti-DLC3 from right to left, roughness, adhesion and friction. 57
Fig. 41. The home window of the JPK software used to monitor and control the measurement process. 57
Fig. 42. The Gwyddion main and user guide windows [61]. 58

List of tables

Table 1. The elemental atomic percentage of the films measured by XPS [27]............................... 22
Table 2. The deposition parameters of the DLC films... 29
Table 3. Cantilevers technical data, Nominal values and specified ranges [29, 31, 52].................. 31
Table 4. The technical data of the Raman spectroscopy... 37
Table 5. The roughness parameters, Skewness and Kurtosis, as well the Hurst component H and the fractal dimension D_f of each sample.. 39
Table 6. The average values of the elemental weight and atomic percentage of each sample. 41
Table 7. The average values of the elemental atomic concentration renormalized without the silicon element. 41
Table 8. The samples adhesion parameters values from the Quantitative Imagining operation mode data. 45

List of abbreviations

Abbreviations:

MSD – Magnetron sputtering deposition;

PVD. – Plasma vapor deposition;

CVD – Chemical vapor deposition;

PECVD – Plasma enhanced chemical vapor deposition;

PLD – Pulsed laser deposition;

FCVA – Filtered cathodic vacuum arc;

IBSD – Ion beam sputter deposition;

Ti-DLC – Titanium doped diamond-like carbon;

DLC – doped diamond-like carbon;

AFM. – Atomic force microscopy;

KeV. – Kilo electron volt;

DC. – Direct current;

RF – Radio frequency;

XPS – X-ray photoelectron spectroscopy;

SEM – Scanning electron microscopy;

EDS – Energy Dispersive X-Ray Spectroscopy;

QI – Quantitative imagining;

RMS – Root mean square roughness;

RS – Raman spectroscopy;

Introduction

Nowadays, the deposition technology becomes excessively exploited in broad domains, such as medical implants (hip joint, artificial cardiovascular devices, knee replacement) [1-5], automotive industry (engines components, pistons, pumps coatings) [6-9], as well everyday tools (kitchen knives, drill bits, razor blades) [10, 11], and many others.

Recently, the successes of such technology pushed the scientists to go further in research to improve the coating quality and adopted it in new applications. In the begging, the diamond-like carbon (DLC) thin films were coated on wanted surfaces to enhance mechanical properties as the hardness, modified the optical or tribological properties. This was usually done using different types of deposition techniques such as the magnetron sputtering deposition (MSD), the plasma vapor deposition (PVD), the pulsed laser deposition (PLD), Filtered cathodic vacuum arc (FCVA), the Ion beam sputter deposition (IBSD).

Newly, various metals such as (Ti, Cr, Zr, Ni, Au, Ag) as well non-metals elements (Si, O, N, F) were excessively used as doped materials in the diamond-like carbon (DLC) films. Each dopant has its role in modifying the film structure and, as a consequence enhancing a desirable property for different DLC film types and in several application domains [12-14]. The doping process of DLC films with titanium has repetitively demonstrated its enhancing role of the tribological and mechanical characteristics, like reducing the compressive stress, friction coefficient and enhancing the corrosion and wear resistance, additionally improving the hardness [12, 15]. However, the structure and properties of Ti-doped DLC films very strongly depend not only on the Ti amount but also on the process parameters and the used technology in the deposition.

In this work, the objective was to deposit the titanium doped diamond-like carbon films using magnetron sputtering and determine the films' structure and properties. For the sake of achieving this goal, the following tasks were set:

1. Synthesized the diamond-like carbon films with different concentrations of titanium.
2. Investigate the influence of Ti content on the structure of the sputtered films.
3. Evaluate the surface morphology parameters of films by atomic force microscopy analysis.
4. Determine the lateral deflection signals (friction force) and optical transmittance of the Ti-doped DLC films.

1. Magnetron Sputtering Deposition Technique

The Magnetron sputtering deposition is a technique developed, in the 70s of the last century, from the sputter deposition, which is a physical vapor deposition (PVD) method of a thin film deposited by sputtering. This technique is considered as one of the most dominant mechanisms in the thin films deposition domain. This is due because of several reasons, such as the simplicity of its equipment, the ease of deposition process control, the large coating area which can be achieved, and the strong adhesion which can be obtained. These main advantages allow the preparation of large quantity of thin films from metal, metal oxides to diamond-like carbon at relatively high purity and low cost in several applications [16].

1.1. Fundamental & concept of Sputtering process

By definition, sputtering is when particles such as atoms, ions, or clusters get ejected from a target's surface, which is usually done through bombardment by energetic ions. Two types of sputtering, “chemical” and “physical,” can be distinguished. In the physical sputtering, the energetic ions usually have enough energy to penetrate inside the surface of the target material to a certain depth after following cascades collisions or thermal spikes. The process can be seen in **Fig. 1** below [17]. In the literature, usually, the word “sputtering” refers to the physical type.

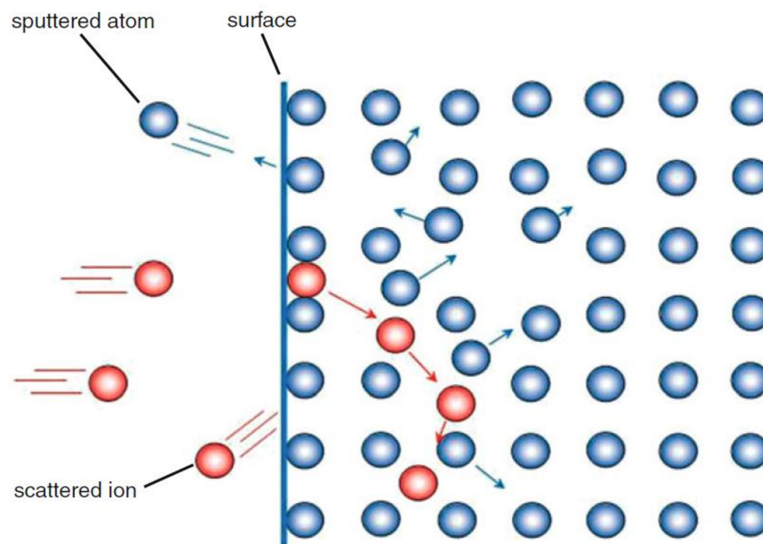

Fig. 1. The sputtering process schematic [17]

As seen in **Fig. 1**, when energetic ions bombard the target atoms, these atoms gain energy and begin to move in a particular direction. If an atom moved toward the target surface and if it had enough energy to exceed the surface binding energy after reaching this surface, it can then eject (usually, the initial energy value is about 3 to 4 times greater than the binding energy between the surface target atoms). It will be called a sputtering atom. It should be noted that some energetic ions get scattered from the target's surface; consequently, they do not engage the sputtering process. As a consequence, the term "sputtering yield' is defined as a ratio that equals the number of the ejected atoms divided by the number of incident ions (including the different types of ejected particles). In other words, the "sputtering yield" measures the efficiency of the sputtering.

This efficiency is affected by many parameters such as [17]:

1. The mass and the energy of the incident ions;
2. The angle of incidence;
3. mass of the target particles;
4. The temperature of the process;
5. The bombardment dose, and so on.

Several measurements, such as in Behrisch et al. [18], Andrew H, Simon [19], and G.K Wehner [20], have been performed to determine the effects of these previous parameters on the sputtering yield considering different ions-target combinations, the condition of the surface, and the orientation of the crystal target. Since 1926, the early theories mostly had the idea of the arbitrary direction of the sputtered particles. The authors believed that the sputtering process is produced due to the incident ions penetration and their energies delivered in the target mesh until G.K Wehner found that the directions of the sputtering are not arbitrary in every direction by using a single crystal. The confirmation on this discovery came up when the experimental results showed that the maximum expulsion velocities and the average are too high, which cannot be explained with the pure evaporation mechanisms [20].

P. Sigmund [21] had developed one of the most important theory for the amorphous materials, which indicates that the sputtering yield S(E) for an energetic ion with an energy E exceeding 1 KeV can be written as follow:

$$S(E) = 3/4\pi^2 \times 1/C_0\, U_0 \times \alpha \times S_n(E) \quad (1)$$

Where C_0 is a parameter obtained by the interaction potential of the target atoms at rebound energies, U_0 is the potential barrier of the surface (the surface atoms binding energy), α is a parameter related to the efficiency of momentum transfer in the hitting, and $S_n(E)$ is the elastic stopping power given by J. Lindhard et al. (1968) [22]. In the case where the energy of the incident ions is less than 1 KeV, the sputtering yield becomes:

$$S(E) = 3/4\pi^2 \times \alpha \times T_m/U_0 \quad (2)$$

Where $T_m = 4M_1M_2/(M_1M_2)*E$ is the maximum energy transfer. M_1, M_2 are the mass of the arriving ion, the target particle, respectively. The sputtering yield changing with the incidence ion angle θ to the target surface was also given by P. Sigmund [23]:

$$S(E,h) / S(E,1) = (\cos\boldsymbol{\theta})^{-f} \quad (3)$$

Where h is the direction cosine, S(E,1) the sputtering yield for normal ion incidence, and f is a number limited between 1 and 2.

1.2. The concept of Magnetron Sputtering and its configurations

Generally, to adopt the sputtering process as a method for deposition, it is necessary to elevate the sputtering yield number or the number of the target atoms in the plasma and then direct these atoms to be deposited on a substrate. The following can be done by introducing a Magnetic field, as illustrated in **Fig. 2**, where three large magnets (usually permanent magnets) are located behind the target material (commonly with a cylindrical shape), and the lines of the magnetic field B_p can be seen.

Additionally, the two surfaces (the target or cathode and the substrate or anode) are held on two different voltages, the negative potential $-U_T$ and a lower negative potential $–U_B$, respectively. This discharge voltage can be maintained by a DC high voltage or by RF (radio-frequency) to ensure an alternating potential or using an HF (high-frequency) supply to initiate the magnetron discharge. The last step is required to produce an electric field perpendicular E to the magnetic field. In **Fig. 2**, the configuration should be placed in a vacuum chamber of about (10-3 Pa) [17]. Also, another condition is required to start the deposition process, which consists of introducing a suitable gas, normally argon, controlled by a gas regulating system. The “Glow discharge” appears due to the high voltage; this high voltage starts to ionize the argon gas, where the electrons and the ions are apart. The presence of the magnetic field B_p and the electric field E affect the motion of the free electrons created by a derived force F, as written below:

$$F = -q \times (E + v \times B_p) \tag{4}$$

Where q is the electron charge and v is its velocity. There are two cases to discuss the motion of the electrons. Firstly, if these electrons are emitted in a perpendicular direction to the target and parallel to B and E vectors, the term v x B_p in Eq. (4) will be annulated. These electrons are affected by the electric field E, so they depart from the target surface, which is negatively charged. The other situation is where the magnetic field lines B_p and the target are parallel to each other and perpendicular to the electric field E; here, the electrons become besieged in the E x B_p field in the region above the surface of the target. This situation allows each electron to hit a massive amount of argon gas atoms. This area is named “dark space,” and it is necessary to enhance the ionization of the argon gas.

Meanwhile, when argon gas begins to be ionized, the electric charge E accelerates these positively charged argon ions, which are created after the collision with the electrons, toward the target. Hence, the sputtering process will be maintained. As it is seen in **Fig. 2**, depending on the configuration, for example, when the magnetic field lines end at the central south pole before starting from the two north poles on the sides, this configuration is known as the Balanced Magnetron Sputtering (where the magnets have the same strength). Another configuration called the Unbalanced Magnetron Sputtering (where the outer magnets are more powerful than the central magnet) can be observed in **Fig. 3**.

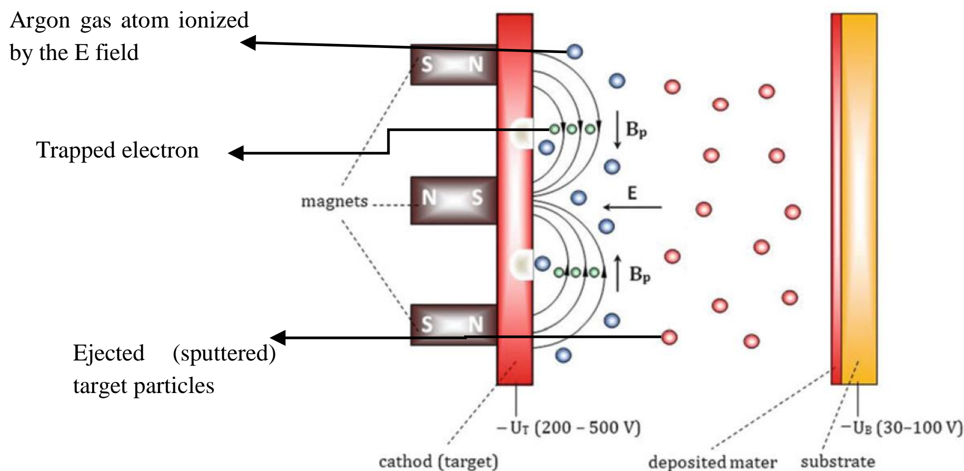

Fig. 2. Illustration of the Magnetron Sputtering Deposition [17].

In an unbalanced magnetron sputtering, as the magnet in the center is weaker than the magnets in the outer, a part of the magnetic field lines of the magnetron becomes open at the end, so they do not close the loop with the other magnetic lines. Thus, the plasma is extended up to the substrate, and this lets the argon ions bombard the initially created layer. Simultaneously, this leads to enhance the sputtering rate as the ions separated from the surface are accelerated to the substrate. Some simulation software already created can help in calculating the optimum magnetic configuration [17]. As previously mentioned, magnetron sputtering can be designed in various types, such as radio frequency (RF) magnetron sputtering and direct current (DC) magnetron sputtering. Theoretically, the RF magnetron sputtering allows the deposition of any material without the necessity to be an electrically conductive material.

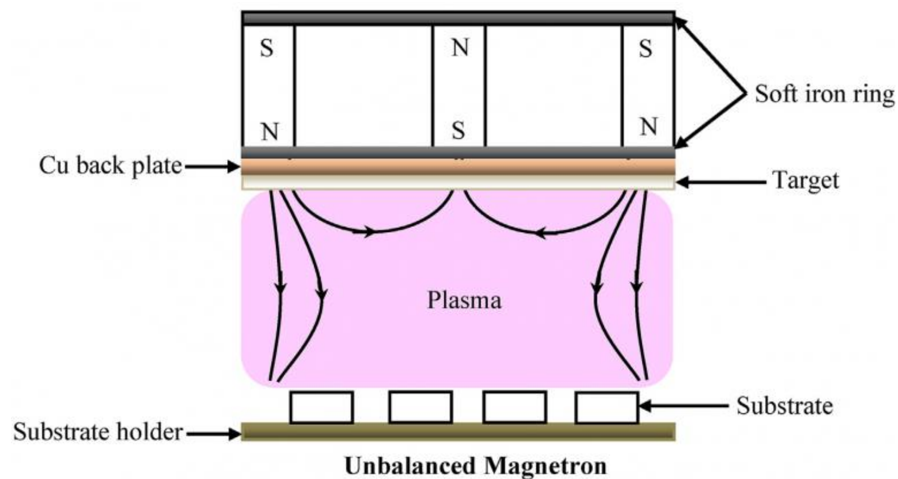

Fig. 3. Unbalanced Magnetron Sputtering configuration [24].

1.3. Technical description and some key features

Technically, the magnetron sputtering deposition device a schematic as shown in **Fig. 4**. A broad diversity in the designs and the construction can be existed depending on the objectives and the applications. Some articles studied the optimum design for specific applications [25]. Also, in this article [26], the improvement of the target life and the acceleration of the deposition time was obtained by performing an active compensation magnetization and an appropriate passive iron annulus in the DC Magnetron Sputtering.

Firstly, regarding the substrate, its voltage should be a negative potential as well be held in the range of (-30 to -100 V) [17], this condition allows the bombardment to be happening at the most productive ion energies (the interpretation will be in the next part). Secondly, about the substrate design, the purpose of having a rotating substrate holder is to obtain an optimal coating thickness as well homogeneous. The following design provides such improvement [17].

Regarding the utilized power value between the cathode and the anode, an initial high negative voltage is typically applied in the range of -1 KeV or higher. Then, the magnetron voltage is kept at approximately -200 to -600 V during the sputtering process. Some modern power supplies have automatic voltage regulation, preventing the ultimate electric breakdown on the target surface. Nevertheless, this requires an automatic electronic arc handling system [17]. For the pressure condition, the vacuum has to be held at a constant value of about 10 to 3 Pa during the whole deposition process.

The latter is an important step to deliver the driving gas, typically argon or other gas such as O_2, N_2, C_2H_2, CH_4, depending on the type of formed films. In general, the operator keeps the gas at a pressure range of 1 to 5 Pa via a highly accurate gas flow regulation system. As the sputtering rate is variate and the pump efficiency is not stable, the gas flow rate must be modified during the deposition process. This adjustment can be accomplished by automatic systems controlled by computers in modern designs.

Undoubtedly, the temperature is one of the most crucial parameters that must be controlled before and during deposition to release all the possible existing besieged gases (nitrogen, oxygen, and hydrogen) from the metallic materials (substrate). Consequently, this leads to a lower adhesion, which is an undesirable property in the coated film. To prevent this issue, using the high vacuum condition is necessary to evacuate these gases, together with a temperature around 100 to 400 0C should be insured [17], the values of these parameters are limited depending on the coated material and the type of coating used, considering the deformation risk which may occur.

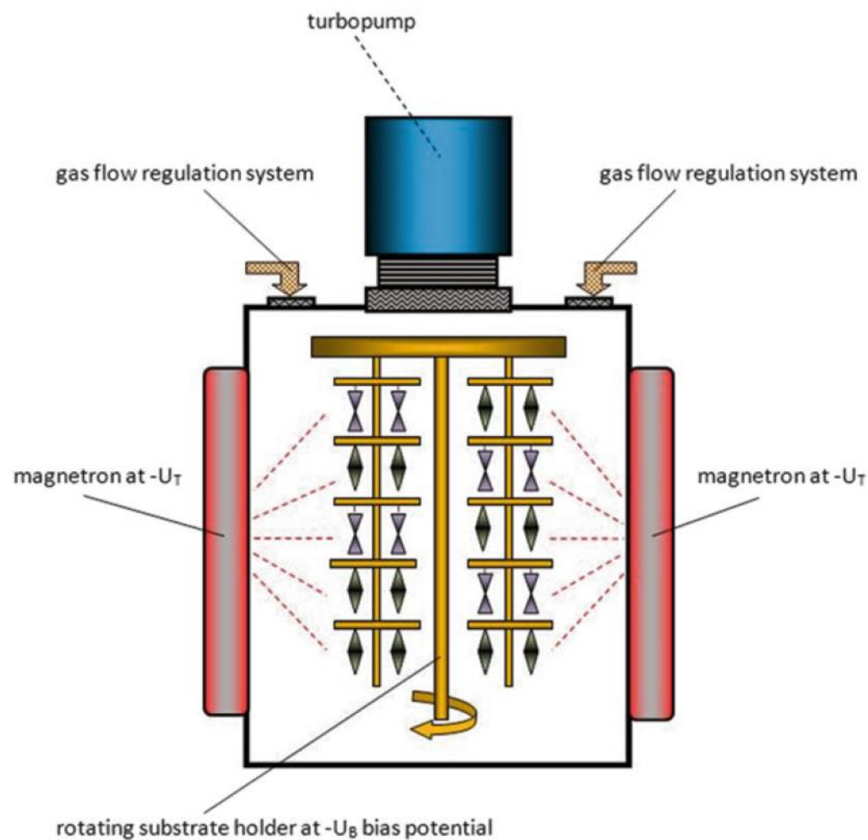

Fig. 4. The principal components of a magnetron sputtering deposition device [17].

On the other hand, a lower range of 100 to 300 ^{0}C is usually selected for the temperature during the deposition. The importance of this regulation is to obtain an excellent chemical reaction rate and film quality. One important particularity, which should not be taken lightly, is applying well cleaning procedures before the deposition process, especially in consecutive coating processes. This is because any impurities, like dust or previously contaminated particles, will affect the purity of the thin film being deposited and, consequently, prevent the desired coating properties.

2. Diamond like Carbon Thin Films

This chapter contains the following points: In the first section, a short review about the Diamond-like carbon thin films, such as: what is a DLC thin film, their classification, characteristics, applications, and utilization. In the second section, a board review from the recent studies about the effects of the doped elements on these thin DLC films, especially the titanium, such as their morphologies and topographies, their mechanical properties such as hardness, roughness parameters, adhesion, friction coefficients and so on…as well some future improvements in the chemical and biological domains.

2.1. Classification of DLC films and their types

Generally, from the carbon phase and the hydrogen content perspective, there are DLC films types, (a-C) which is stands for the free hydrogen film, hydrogenated carbon (a-C:H), tetrahedral amorphous carbon (ta-C), hydrogenated tetrahedral amorphous carbon (ta-C:H).

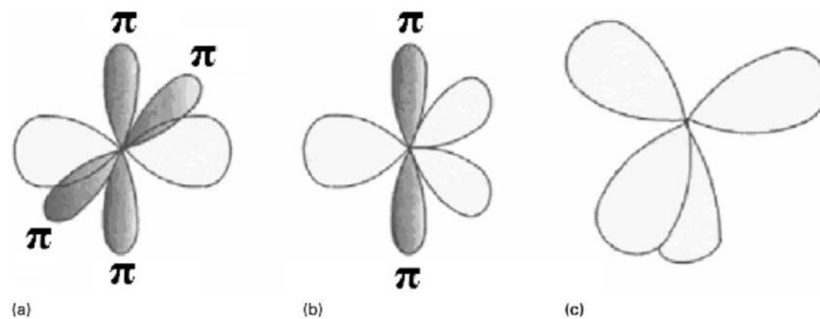

Fig. 5. (a) sp^1 (b) sp^2; (c) sp^3; carbon bonding configuration [41].

Additionally, other types can exist with silicon, oxygen, nitrogen, or other elements dopants. The main difference between the DLC film types is the portion of sp^2 and sp^3 of the carbon bonds. The ratio sp^2/sp^3 influences the DLC films' optical, electrical, mechanical, and tribological properties. The electrons in a ground state carbon atom exist essentially in three possible configurations (sp^1, sp^2, or sp^3) **Fig. 5** [40].

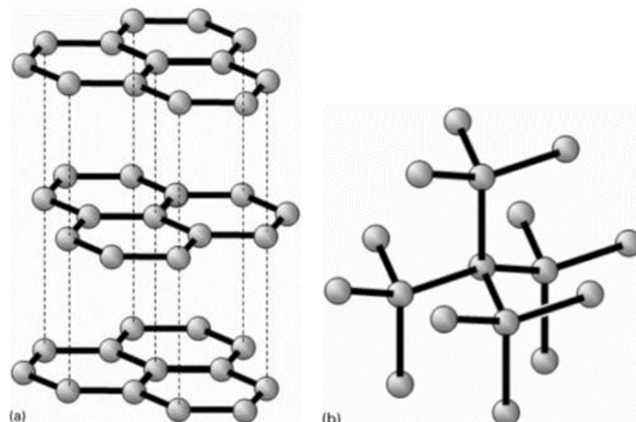

Fig. 6. From the right, the graphite and the diamond structure of carbon atoms respectively [43].

Mainly, the carbon atoms form the graphite structure as the sp^2 configuration bonds, which have strong bonds between the atoms in each plane, but the bonds between the planes are weaker since they are van der Waals type. Generally, the bonding energy is 7.4 eV; however, it is only 0.86 eV

between planes [41]. That gives intensely mechanical properties within a layer for the graphite. However, it is not the case between the layers; consequently, they can be separated easily.

Moreover, the diamond structure is formed by the carbon atoms that existed as the tetrahedral sp^3 configuration bonds. In this case, the carbon-carbon bond lengths are short, around 1.54 Å [40], with high bonding energy of about 3.26 eV per bond [42]. **Fig. 6** illustrates the three-dimentional structures for both cases, graphite, and diamond. The diamond-like carbon thin films are regularly structured from tiny crystallites with either sp^2 or sp^3 configuration. Any electron diffraction technique can be used to investigate the amorphous material. As J. Robertson shows [40], the carbon films are affected by the sp^2 and sp^3 bonding portion and the hydrogen content inside the films.

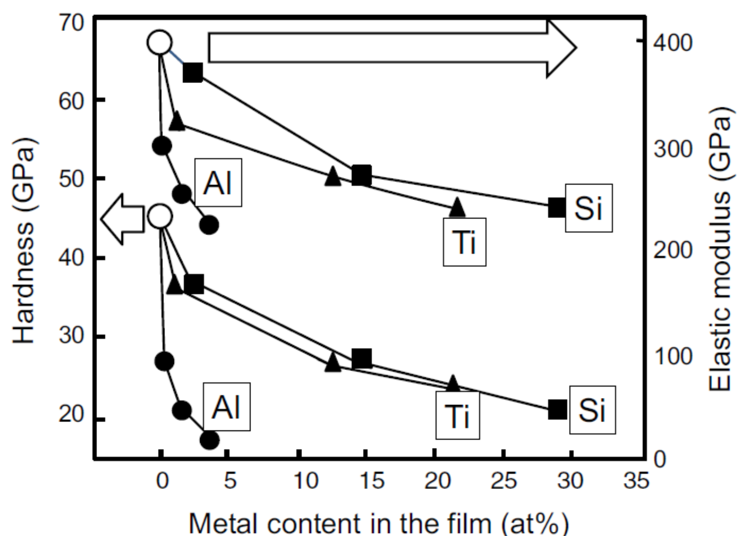

Fig. 7. The variation of the and the elastic modulus and the hardness with the concentration of three different dopant metals in the DLC thin films, deposited by FCVAE [58].

Primarily, the purpose of the DLC films is to provide the coated surface unique properties to improve its performance in such applications. Additionally, improving the DLC film properties and extending the application areas through the doping process is possible. (some used dopants are: Si, Al, Ti, N, and Ag) where each doped material can have a specific effect on such property. It was stated that wetting behavior improved with Al dopant, where the highest contact angle of 101° was observed with water contact [53].

Also, the metal dopants excessively change the electrical properties, where the electrical resistivity was very low ~10^{-2} Ω.cm [54, 55]; the optical property changes by using N dopant and bioactive properties by utilizing Ag dopant. **Fig. 7** illustrates how the hardness is changing versus the increasing of different elements concentration. It is noticed that the aluminum Al has a significant influence on hardness and elastic modulus of the coating; where these two properties enormously decreased (from ~68 to ~45 GPa and from ~400 to ~230 GPa respectively for hardness and elastic modulus) with the addition of a small amount of Al (less than 5 at.%). However, for the titanium Ti and the silicon Si, the sufficient quantity needed to produce a similar effect was more than 22 at. % and 29 at. % for the Ti and the Si, respectively.

2.2. Raman spectroscopy for characterization of DLC films

Generally, Raman spectroscopy is used to characterize the carbon phase basing on the Raman effect with other investigation techniques. Theoretically, when the light interacts with a material, various kinds of interactions can happen. Several factors contribute to making one interaction type dominated over the other, like the wavelength of the light, the shape and the size of the particles of the material, and the type of interaction, which could be elastic or inelastic. The Inelastic scattering such as Brillouin scattering and Raman scattering by molecules or phonons are examples of the reflected light changes.

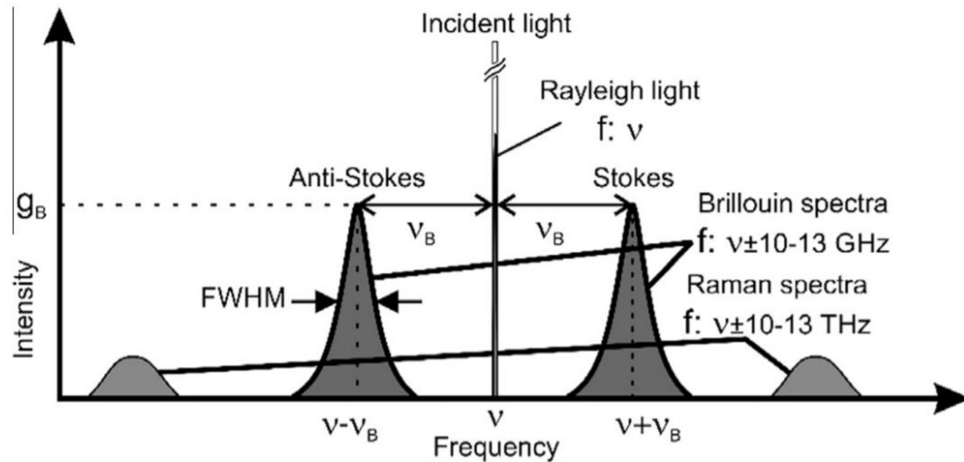

Fig. 8. A typical spectra of scattered light in optical fiber [57].

Theoritically, Raman interaction is an inelastic process, which means that the photon can either lose or gain energy. The case where the photon loses energy is named the Stokes process; it consists of three subcases, depending on the quasiparticles created: phonon, magnon, and polaron. The opposite case is defined as the anti-Stokes process, where one of these three previously mentioned particles is absorbed The creation of phonon is called mass oscillation, for polarons is named charge displacement, and for magnon is known as magnetic spin oscillation. The amount of phonon energy shifts the Rayleigh line frequency to a higher or lower value depending on the stokes or anti-stokes case. So this phenomenon allows using Brillouin scattered light to measure the energies wavelength and frequencies of several atomic oscillations. **Fig. 8** illustrates the Rayleigh, Brillouin, and Raman spectra for optical fiber [57].

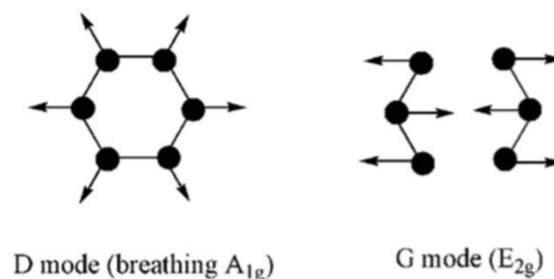

Fig. 9. The carbon atoms' vibration mode. From the right, the breathing A_{1g} mode represents the D-peak, the stretching E_{2g} mode stands for the G-peak [59].

Usually, the Raman spectra shape of the DLC films depends on the nature of the film and provides essential information about the structure. Two peaks for DLC films mainly appear in the visible excitation at about 1560 cm^{-1}, 1360 cm^{-1}, and one peak in UV excitation at ~1060 cm^{-1}. These peaks are known as the G, D, and T peaks, respectively. In **Fig. 9**, on the right, the stretching mode stands for sp^2 atoms in both rings and chains, which makes the G peak appears [44]. The breathing modes of rings cause the D peak to be presented, while the T peak is due to C–C sp^3 vibrations (see **Fig. 9**). Commonly, the visible laser is used as an exciter in Raman spectroscopy. However, using a multiwavelength in the Raman spectroscopy could be justified when providing additional information is required. Besides, depending on the Raman cross sections for sp^2 or sp^3 carbons, this action can introduce unwanted peaks on the spectra, or the dispersion behavior could cause the bands to be merged due to the resonance phenomenon [45].

Basically, the transformation from graphite (0% sp^3) to the ta-C phase (100% sp^3) can be explained by the three-stage model of bonding and ordering the carbon atoms. These three stages are [7] [8]: (1) Graphite to nanocrystalline graphite; (2) Nanocrystalline graphite to sp^2 a-C; (3) a-C to ta-C (until 100% sp^3 ta-C, impure diamond). The Raman spectra are depending on: (1) The accumulation of the sp^2 phase; (2) The bond length and bond angle disorder. (3) The existence of sp^2; (4) The sp^2/sp^3 ratio. The right part of **Fig. 10** illustrates the Raman spectra of the typical carbon film types, as well the D and G peaks appearing. In the DLC films case, mostly the spectra will have the a-C:H shape with other peaks that could appear.

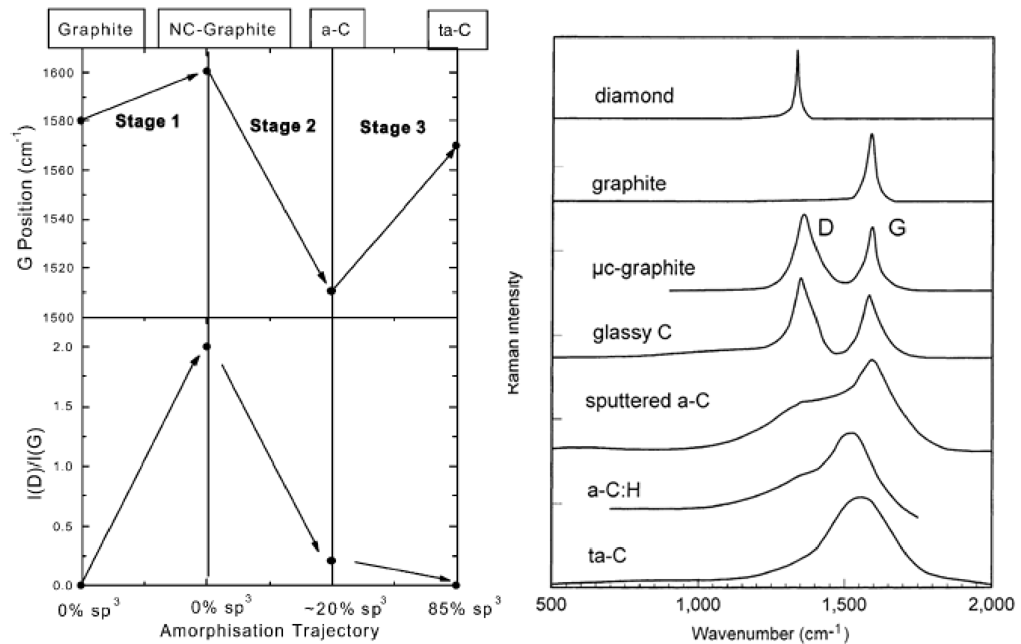

Fig. 10. On the left, the amorphization trajectory, shows the G position variation as well the peaks intensity ratio with 514.5 nm excitation versus the sp^3 amount. On the right, the Raman spectra of typical carbon films [44, 63].

In summary, the carbon lattice disorder is indicated from the D peak parameters, depending on the stage at which structure the DLC film has existed. More disorder in graphite leads to an increase in the D peak intensity, as seen in first stage. Also, more arranging in amorphous carbon and in nanocrystalline could be revealed by the D peak as seen in the second and the third stages. As a result,

the quality of graphene ultrathin films could be estimated from the I(D)/I(G), where a lower ratio indicates a high-quality order [2]; also, this could be an indirect way to indicate the sp^3, since the degree of disorder is related to the sp^3 in the seconf and the third stages [46].

An overview of the three stages demonstrates that the relationship is not stable between the sp^3 content and the G peak position in the whole amorphization trajectory. The trend of the G peak can be used to determine at which state of amorphization the DLC film has existed. However, depending on the I(D)/I(G) variation, if the G-peak position and I(D)/I(G) are directly proportional thus, the sample could be at the first or the second stage. Then depending on the G-peak position (if less than 1581 cm^{-1}, this refers to the second stage), while if they are inversely proportional, then the sample is in the third stage).

2.3. Applications and utilizations

The DLC and doped-DLC coatings provides unique characteristics, and this allows it to be widely prevalent in several areas, significantly reducing wear resistance and sliding friction. Also in the production of tooling components, such as end mills, drill bits, the razor blades such as the Gillette is one of the most known DLC application. The exploit of DLC coatings expanded to other applications like the pistons, bearings, pumps, and automotive industry elements such as gears and shafts, as shown in **Fig. 11** [6] to enhance the engine performance. In 2001, the estimation of the coated parts production was nearly 30 million in the automotive industry each year. This percentage would rise by 50% per year [7]. An Ion beam-assisted deposition was performed to coat components of an engine, as reported by J.H. Arps et al. [8], where an intermediate layer of silicon was coated to evolve adhesion by forming a metal silicide.

Fig. 11. Automotive components with DLC deposition [9].

Likewise, the DLC film with low corrosion resistance and biocompatibility allows surgeons to use it in biomedical implant applications such as coatings for hip joints and knee replacement [37, 2]. In this case, the coatings require high quality with excellent adhesion, well surface finish [3]. Furthermore, in the medicine domain, the DLC has been used to coat biosensors and cardiovascular devices [4]. The diamond-like carbon (DLC) has been used as a biocompatible coating in orthopedic and cardiac medicine [47].

In addition, the DLC films have their presence in the fluid technology, such as the coating of the ceramic plate (which is used as a seal) by stiff hydrogen-free a-C. The friction value was reduced

from 0.4 to 0.04 for the ceramic–ceramic contact, as the Delta Faucet Company [10] claimed. Moreover, applying the ta-C thin films could multiply the lifetime of the kitchen knife coating by a factor of 10, according to this paper [11]. The knives' improvement was clear after applying a coating with 1.5 µm, where the hardness became ~ 55 GPa (five times higher than the blade's steel). As well the lifetime of coated knives is significantly improved comparing to the uncoated knives.

2.4. Titanium doped diamond-like carbon films

Various metals (Al, Ti, Ag, Zr, Au) are used to improve the properties of the DLC films [13]. Titanium is one of the dopants used to change the structure of the DLC films and is mainly used to enhance the mechanical and tribological properties of the films [27, 28, 32, 36]. The Ti-doped DLC films are produced using various deposition techniques such as plasma physical vapor deposition (PVD) and chemical vapor deposition (CVD), magnetron sputtering deposition (MSD), ion beam sputter deposition (IBSD), filtered cathodic vacuum arc (FCVA), or the pulsed laser deposition (PLD). Also, it should be noted that the synthesis parameters and titanium amount are the key factors affecting the films' final properties.

Table 1. The elemental atomic percentage of the films measured by XPS [27].

CH_4 (sccm)	Ti content (rel. at.%)	Si content (rel. at.%)	C content (rel. at.%)	O content (abs. at.%)
10	30.3	6.8	62.9	23.0
20	18.8	3.6	77.6	8.3
30	9.5	2.2	88.3	6.6
40	4.5	1.0	94.5	6.4
60	0	0.5	99.5	2.4

Firstly, in W. Liu et al. study [27], five doped DLC films were deposited by changing the CH_4 flow rates. It was indicated that the increasing CH_4 flow rates lead to a decrease in the Ti amount from 30.3 at. % to 0 at. %, Si content from 6.8 at. % to 0.5 at. %, as well oxygen from 23 at. % to 2.4 at. % in the films (see **Table 1**). The Raman analysis shows that as the CH_4 flow rate augments from 10 sccm to 60 sccm, the G band shifts from 1549 cm^{-1} to 1557 cm^{-1} and then to 1544 cm^{-1} and I(D)/I(G) went up from 0.68 to 1.34 and then to decreased to 0.56. The RMS surface roughness decreases from 6.50 nm to 0.68 nm with the decreasing Ti content from 30.3 at. % to 4.5 at. %, while it remained constant until pure DLC. The friction measurement was done in ambient air; the lowest friction coefficient 0.0139 was achieved when the Ti and Si contents are 4.5 at. % and 1.0 at. %, respectively **Fig. 12**. In conclusion, the lowest friction coefficient was achieved at a CH_4 flow rate of 40 sccm, where the film has a modest sp^3 content.

Regarding G. Ma et al. article [28], two coatings, one with pure carbon target and the other with titanium doped, were performed. The elemental analysis indicates that a 93 at. % C, 1.7 at. % O and 5.3 at. % Ti. The sp^3 fraction in the pure DLC film and Ti-DLC coating was about 40.2 at. % and 33.0 at. %, respectively. The cubic TiC nanocrystalline clusters in **Fig. 13** are structured as an amorphous hydrocarbon. Thus, the nanocomposite DLC phase are embedded in the coating. The Ti-doped was significantly stiffer than the unmodified DLC film. Furthermore, a ~35 N critical load was measured in the Ti-doped DLC, which is much higher than the unmodified DLC ~7.5 N. An additional measurement was done on a TiC transition layer between Ti-doped DLC and Ti alloy

substrate by ion implantation. This measurement demonstrates a higher value of the critical load, which is the highest among the three samples, around 60 N.

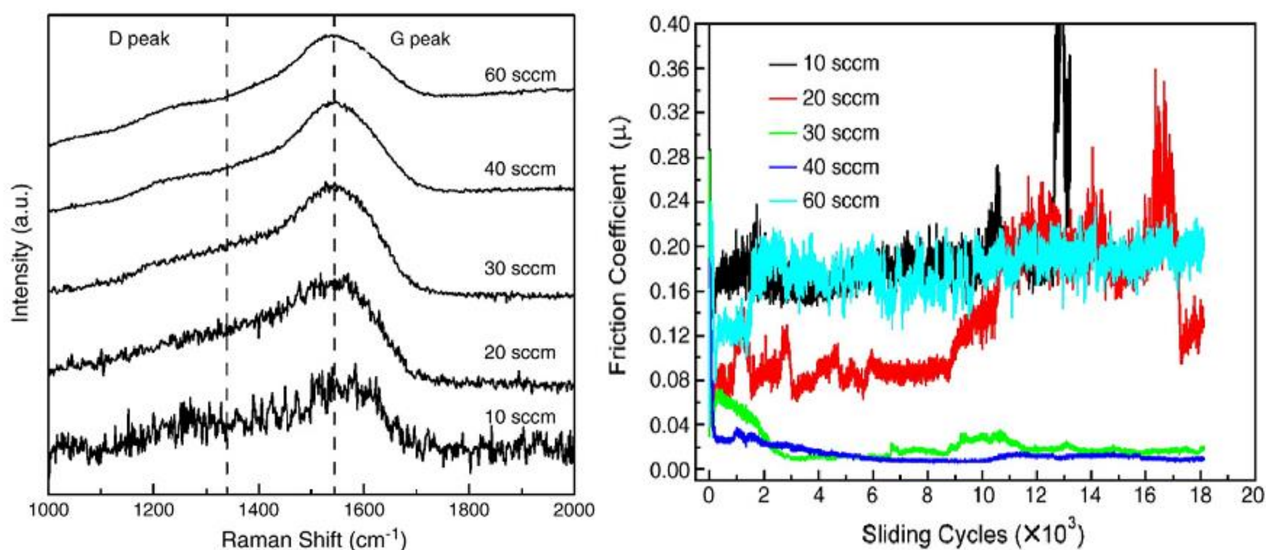

Fig. 12. The Raman spectra of the films and their friction coefficient [27].

According to J. Zhang et al. paper [15], it was revealed that the Ti concentration in the film increase from 0 at. % to 8.2 at. % with the increase of the Ar/CH_4 flow rate from 0 to 140/110. Meanwhile, at the same range, the XPS and the Raman results (see **Fig. 14**) reveals that the sp^2/sp^3 ratio increases from 2.5 to 5.175. Also, the G peak position shifted to a higher wavenumber as well the intensity peak ratio I(D)/I(G) slightly increased from ~0.83 to ~1.1 (see **Fig. 15**). At 60/190 of Ar/CH_4 flow ratio, Ti concentration was still too low at nearly 0.41%, the film has high hardness ~13.75 GPa, and low stress about 0.55 GPa TiC phase was not formed yet. Despite that, the Ar gas portion increasing makes the hardness decreased from 13.75 to 10 GPa, and the internal stress increased from 0.55 to 0.7 GPa, due to the formation of the TiC phase. An excellent tribological property was achieved at low Ti concentration; the wear rate is nearly 50 times lower than the DLC wear rate, the friction coefficient was much lower, ~0.05. (see **Fig. 17**). It was confirmed that at too low Ti content, the internal stress was the lowest while the hardness remains unchanged, as well an excellent wear resistance and a lower friction coefficient were achieved.

Meanwhile, L. Huang et al. [30] indicate that the pretreatment with Ti atoms enhances the adhesion, where this method was exploited to etch the substrate surface. The bias voltage was adopted to adjust the sp^3 content; its increasing leads to higher sputtering efficiency, raising the sp^3 content and increasing the sp^3/sp^2 from 0.74 to 0.98 measured by XPS. The adhesion strength first increased (from 24 to 31.5 N at 175 and 200V respectively) then decreased to 18.4 N at 300V. The forming of a graphite transfer layer was promoted by increasing the sp^2, which decreases the friction coefficient in the DLC-Si_3N_4 sample (the friction coefficient value increased from ~0.11 to ~0.18 at 175 and 300 V, respectively). While the oxidation of Ti_6Al_4V produced hard oxides, leading to definite abrasive wear in the DLC-Ti_6Al_4V sample (the friction coefficient value decreased from nearly 0.32 to 0.13 at 300 and 175 V, respectively). The wear rate of the DLC films was linearly decreased with the increase of the sp^3/sp^2 ratio for both samples (for the DLC-Si_3N_4 case from ~2.55×10^{-12} to ~1.28×10^{-12} mm^3/N.m. While for the DLC-Ti_6Al_4V case from ~1.08×10^{-11} to ~4.4×10^{-12} mm^3/N.m).

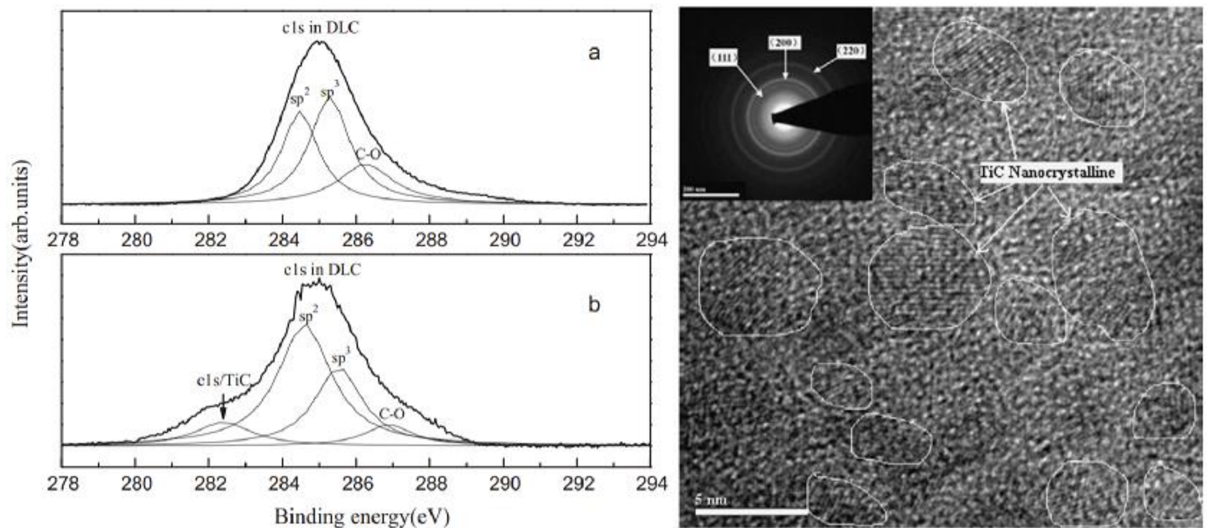

Fig. 13. The XPS and its decomposition spectra. (a) DLC film; and (b) Ti-doped DLC film. On the right, the Ti-doped DLC film TEM micrograph [28].

Moreover, in A. Wang et al. article [32], five Ti-DLC samples were deposited with Ti concentration varying from 3.78% till 23.57%. The Raman results revealed that the I(D)/I(G) ratio slightly decreased from 1.21 to 0.9 at 3.78 at. % and 7.19 at. % of Ti, respectively. The further increase in the Ti content resulted to monotonous increase of I(D)/I(G) ratio till 1.46 at 23.57 at. %. The G peak FWHM trend well agreed with I(D)/I(G) one. So, at first the Ti amount leads to decrease the sp^2 content but then more graphitization make it increase. It was revealed that, when the Ti concentration is between 7.19 at. % and 12.87 at. %, the films tended to graphitize, the compressive stress reduced to ~1.6 GPa, with a lower friction coefficient ~0.13 and likewise the wear rate $\sim 1.2\times 10^{-7}$ mm^3/N.m. However, for further concentration increasing the carbide nano-particles Ti-C were created in the DLC film. This leads to enhance the hardness of the films (from ~22 GPa to ~28 GPa at 23.57% Ti). Also, this results the friction coefficient to reach ~0.25 and wear rate $\sim 1.7\times 10^{-6}$ mm^3/N.m.

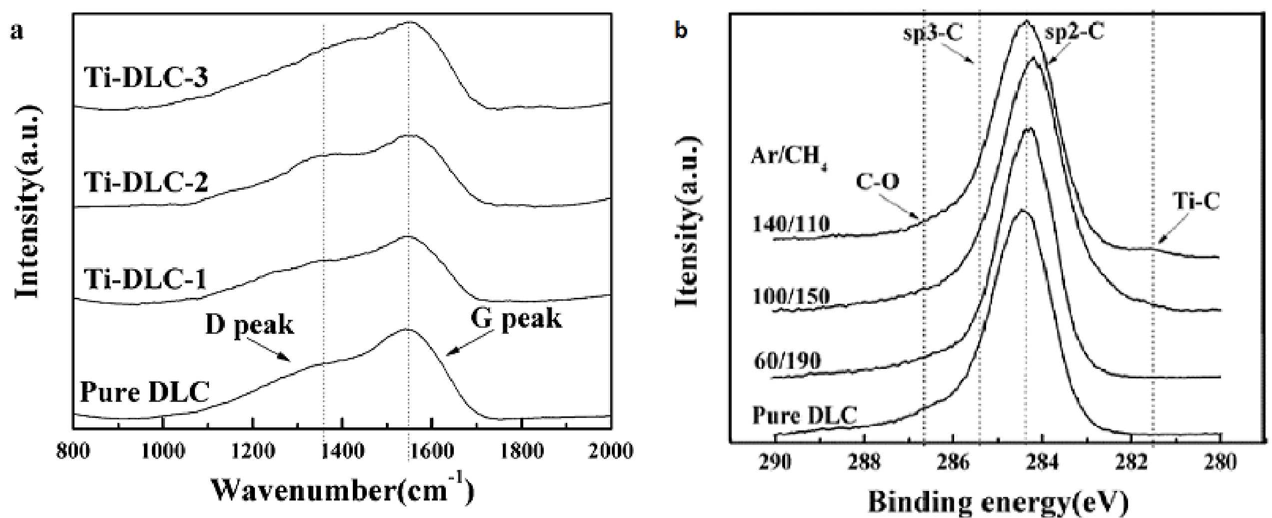

Fig. 14. The Raman spectra of each sample and The XPS C 1s peak of the films with different Ar/CH_4 flow ratios [15].

In K.H. Kim et al. article [33], The Ti content quickly increased from 2.2 at. % to 5.8 at. % with the increment of the Argon flow rate ratio (from 0.85 to 0.94) in the ($Ar/Ar:C_2H_2$) mixture gas by a combined PVD/PECVD deposition process. It was obtained that the surface roughness increased from 5.027 nm to 9.181 nm at 0% and 5.8 at. % Ti, respectively. The sp^2/sp^3 ratio grow up from 1.1 to 2.1 at a similar Ti content range. Also, at low Ti content < 2.8 at. %, the amorphous-phase Ti carbides were formed, and this improves the electrochemical and electrical properties of the films. However, at Ti doping ratio > 4.0 %, the nanocrystalline TiC phase has existed; therefore, the adhesion strength was significantly enhanced.

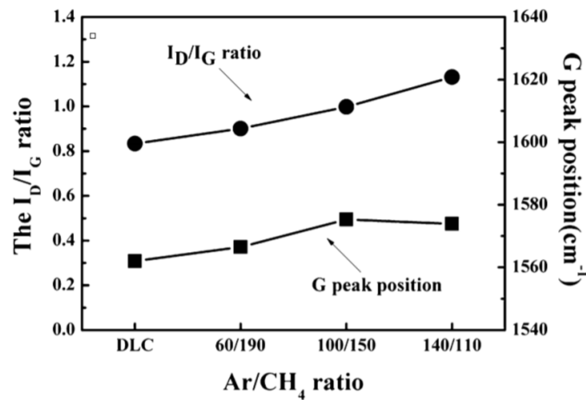

Fig. 15. The G-peak position and I_D/I_G of the films deposited at various Ar/CH_4 [15].

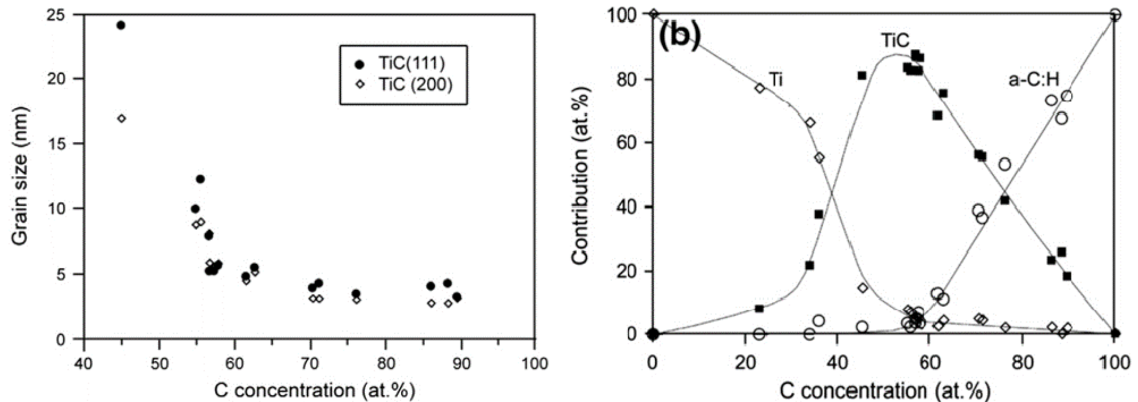

Fig. 16. On the right, the grain size of the TiC versus the carbon concentration. On the left, the percentage of each phases as a function of total carbon concentration [39].

In a recent study by X. Ouyang et al. [36], on Al alloys substrate, a Ti transition layer with a thickness of 0.89 ± 0.16 μm was deposited after a single Ti-DLC layer with various layers' thickness (from 2.4 ± 0.11 to 5.4 ± 0.24 μm). A Ti buffer layer was coated on the top with a thickness of 0.23 ± 0.10 μm, and on the top, a single Ti-DLC was coated again. The C_2H_2 flow rate changing from 10 to 160 sccm leads to a decrease in the Ti amount from ~10.4% to ~1.3%. It is observed that the Ti content range can be divided into three phases. The phase (1), where the hardness increased from 12.17 to 21.43 GPa as the doped Ti content decremented from 10.42% to 8.98 %, in this Ti content range where the polycrystalline composite is obtained, the wear resistance was low between 6.50×10^{-6} and 7.28×10^{-6} mm^3/Nm. The adhesion was between 11.7 and 15.6 N; the friction coefficient increased from 0.53 to 0.77 before decreased to 0.69. Similarly, the elastic recovery first increased from 43.5% ± 1.1 to 46.5% ± 1.9 before a slightly decreasing to 42.6% ± 2.1. For phase (2) with nanocrystalline

composite appeared when Ti content is about 6.06 at. %. Excellent comprehensive properties are obtained, such as high elastic recovery ~69%, high hardness ~23 GPa, high adhesion ~15.6 N, and low friction coefficient ~0.13, and low wear resistance ~1.0×10^{-7} mm^3/Nm. In phase (3), an amorphous composite was obtained when Ti content decreased from 6.06% to 1.35%, the hardness decreases as well from a maximum of 22.23 to 19.85 GPa. This phase composite reveals better wear resistance values between 1.0×10^{-7} and 1.8×10^{-7} mm^3/ Nm, respectively, to the Ti content in this range. While the adhesion linearly decreased from 14.0 to 15.6 N, the elastic recovery was reduced from 69.1% to 63.2%.

Furthermore, in X. Ouyang et al. publication [35], Ti transition multilayers were coated below the Ti-DLC film on Al alloys using the filtered cathodic vacuum arc (FCVA) method. Four different values for the Ti layer thickness were adopted (0; 0.5; 1.1 and 2.8 µm). The G peak FWHM increased from 110 to 140 cm^{-1}, the residual compressive stress was reduced significantly from 12.5 to 2.4 GPa at 0 and 1,1 µm of these Ti transition layers' thickness, respectively. Meanwhile, the hardness decreased (from 25 to 16 GPa) for the same range. Contrary, the elastic modulus, and adhesion show a fluctuation relation. It was concluded that the optimum Ti transition thickness is 1.1 µm with the adhesion of 42.4 N. Besides, C.A. Love et al. reviewed some biological applications such as hip implants possibility of the DLCs coating in their paper [37]. The two critical factors are to reducing wear and corrosion. The review focuses on the hip simulator. Despite the broad range of test conditions, which made the comparison in the literature inconspicuous, the overall results seem positive as an example in DP. Dowling et al. study [38] The wear volume was reduced in the hip joint experiments results (up to 14 times) by deposit a tetrahedral carbon coating. Also, in the pin-on-disc and hip simulator testing, the interlayers improved the coatings.

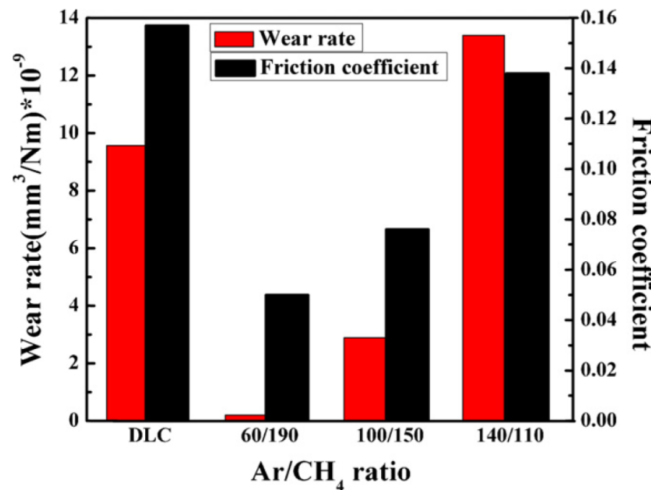

Fig. 17. The average friction coefficient and wear rate variation at several Ar/CH_4 [15].

Additionally, in D. Nataraj et al. article [34], the reactive-biased target ion beam deposition was used to deposit the pure DLC and Ti-DLC thin films. The Ti target bias voltage decrease from -300 to -700V causes the increase of Ti amount in the films from 1.1 at. % to 4.2 at. %. Meanwhile, In the range of at. % Ti from 0 to 4.2 at. %, the sp^3/sp^2 decreased from 0.56 to 0.49, the G peak shifted to a higher position from 1543 to 1568 cm^{-1}, the I(D)/I(G) augmented from 0.8 to 3.1. At 4.2 at. % Ti content, the TiC nanoclusters phase structuring has already begun, and thus the mechanical hardness was reduced. Also, the cell viability test indicates that the lowest Ti concentration film revealed excellent biocompatibility. Moreover, U. Jansson et al. [13] provide a review from the chemical

aspect. The authors summarized how coated films during sputter-deposited (including various elements) could be widely modified in terms of their structure (nearly atomic level), properties (such as friction, hardness behavior, and electrical conductivity). **Fig. 16** illustrates the Ti case.

As seen, regarding the surface roughness (RMS), it slightly increased with increasing Ti content [27, 33]. The friction coefficient mostly fluctuated in several studies [36, 32], where the lowest value of ~0.05 was gotten at 0.41 at. % Ti [15]. One article demonstrated the role of the transition graphite layer in reducing the friction coefficient [30]. The hardness and the internal stress also fluctuated. It was revealed that these two values were enhanced when the TiC phase is formed in the coating matrix [15, 28]. It was obtained that the Ti enhances the adhesion compared to the pure DLC from 7.5 N to 35N, and an additional enhancement can be done by deposit a TiC transition layer to reach the best value with 60N [17]. Also, the lowest at. % Ti of ~1.1 has the best biocompatibility [34].

In summary, the magnetron sputtering deposition technique was frequently used in the literature. Also, this technique was hybridized with other methods like a hybrid ion beam or the filtered cathodic vacuum arc was adopted. The magnetron sputtering provides a high coating area; it can be improved using a rotating substrate holder to maintain a uniform thickness coating along the substrate. Adopting the technique depends on many requirements, such as the material conductivity, where the Radio Frequency type RF is used the non-electrical conductive material. The authors used various deposition parameters to control the dopant amount in the coating most frequently, the argon gas ratio, then methane gas flow rate, and C_2H_2 gas flow rate. Also, the substrate bias voltage was used for the same purpose.

It was noticed that the sp^2 content increases due to a higher carbon amorphization with the increase of the Ti amount in the DLC films. Also, the I(D)/I(G) ratio was slightly increased, and the G peak position shifted to a higher wavenumber with the addition of Ti into DLC. These trends demonstrate the reduction of the sp^3 C-C site content and graphitization of the Ti-DLC films. Such structural changes of Ti-DLC films were demonstrated in the various studies despite different deposition techniques and process parameters. It should indicate that the other elements in the films deposited in these studies were not too high, especially for the oxygen except in the W. Liu et al. [27] case. However, the oxygen amount is too high (reached almost 16 at. % O.); this could be due to the old system available for this work, so more Ti oxide amount was deposited, which is not always desirable. Therefore, these studies do not show how this parameter influences doped DLC films' structural and tribological properties. Also, most of the authors used the ball-on-disc technique and scratching to measure the friction and the adhesion values of Ti-doped DLC films. However, in this research, Atomic force microscopy was adopted to measure these values. This technique is considered the most recent technique and relatively much more accurate. This technique allows the user to measure at the nanoscale, and here the adhesion value is measured between the probe of the AFM and the thin films deposited. It was noticed that these types of measurements, especially at nanoscale, were not previously used to determine the properties of the titanium doped DLC films. Moreover, it should be highlighted that one of the recent studies, which was done by Özoğul A. et al. [56], investigates the relation between the friction force and the actual contact area between the polymer ball probe surface and the SiO_2 surface at nanoscale.

3. Experimental and methods

3.1. Deposition of the doped DLC films

In this project, the magnetron sputtering technique was utilized to perform the DLC thin films using graphite and titanium cathodes. Three substrates, two made out of silicon and one made out of glass, were used in each process. The deposition system used is shown in **Fig. 18**, where the substrate was moving above the targets back and forth at the same altitude.

Fig. 18. The Magnetron Sputtering deposition system photos.

The deposition process was started by preparing the magnetron sputtering system. After turning on the ventilation system, plug in the 3 phases cable to the socket and open the water safety valve. Then the pre-heating step is consisted of these two points:

- Turn on the diffusion pump and then when it reached its maximum load (this can take about 20 minutes).
- Turn on the rotary pump.

The heating pre-step can take about one hour. Meanwhile, prior to each deposition, removing and cleaning the metal parts on the magnets is a mandatory step to eliminate any oxidized element from the previous deposition processes. Then these consecutive stages were followed:

- Insert the silicon (100) and glass substrates into the chamber before closing it.
- Open the valve between the chamber and the rotary pump to start the evacuation process until the pressure reached a low value of ~10 Pa.
- Unclose the other valve between the previously mentioned pumps to start pumping through the diffusion pump.

Once the pressure in the chamber reaches the required value for the deposition, the argon gas was delivered to it. The flow rate can be modified using the controller on the pipe to maintain a stable pressure in the room during the deposition, ranging from 2 to 3 Pa. Then, the deposition process

started by turning on the M1 discharge current bottom. The **Table 2** displays that the discharge current of the titanium was different for each sample, while all the other deposition parameters were fixed.

Table 2. The deposition parameters of the DLC films.

Sample code	Discharge current of Ti target (A)	Discharge current of carbon target (A)	Depostion distance (cm)	Time of the deposition (s)	Argon gas pressure (Pa)
DLC	0	1.5	3	600	2-3
Ti-DLC1	0.25	1.5	3	600	2-3
Ti-DLC2	0.50	1.5	3	600	2-3
Ti-DLC3	1.00	1.5	3	600	2-3

3.2. Atomic Force Microscopy

State of the Art

Atomic force microscopy (AFM) is a widely used technique to investigate at an extremely low scale the height profile of surfaces with different materials. This property distinguishes, the AFM from the conventional microscopes such as the optical and electron, where the vertical dimension at the wanted scale cannot be measured using them. The notable distinction in the function principle overall the traditional microscopes is that the AFM does not rely on the electromagnetic radiation as the measurement means, but instead it uses the mechanical contact to provide three-dimension topography images. **Fig. 19** shows a typical AFM setup and its main components. The height profile could be measured at extremely low scale (up to 0.2 nm and 0.05 nm in the horizontal and vertical resolution, respectively, with a scanning area up to 100 µm) [77].

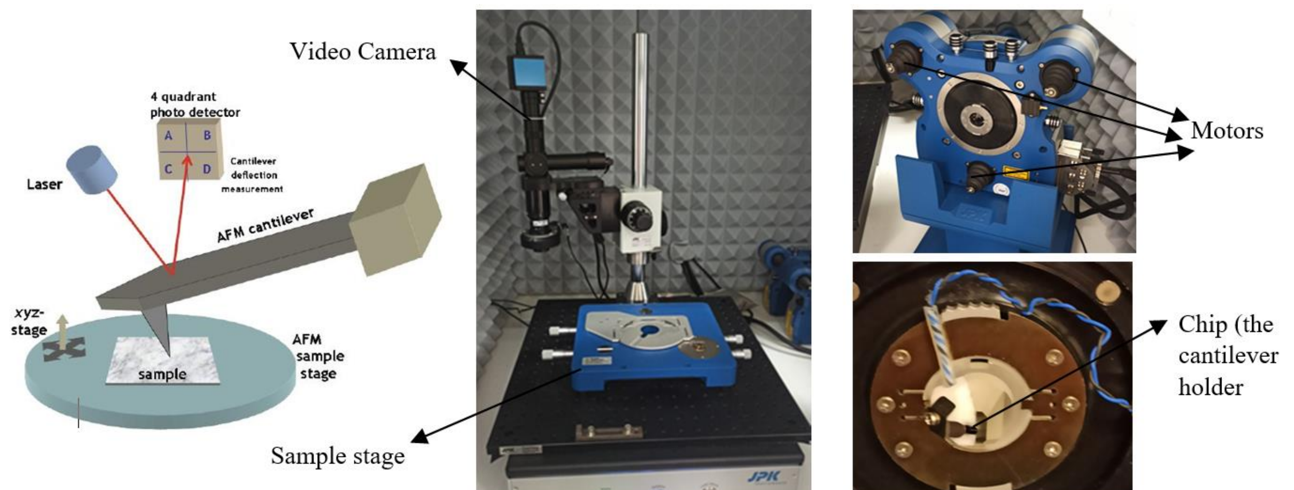

Fig. 19. A typical AFM setup [49] & Photograph of the AFM stage in Jena Otto-Schott institute [48].

A typical AFM consists of the following main components:

– A substrate holds the cantilever, and this last has at its end an extraordinarily sharp and small probe or tip (the newest manufacturing technologies successfully produced which called “tip on the tip” cantilever with the highest sharpness, about 1 nm as tip apex radii [50]. Several cantilevers types and tip shapes are made out of different materials depending on the

measurement purpose (each cantilever has specific technical data provided by the manufacturers, for example, **Table 3**).

– A suitable laser with optical setup to get a sufficiently focused laser spot, usually an infra-red laser. The beam diameter must be much smaller than the cantilever width, nearly 50 µm. The lowest beam diameter that can be released is roughly equal to half of the laser wavelength).
– Quadrant photodetector diode. The idea behind four separate detection areas on the detector is to allow the AFM to be sensitive to any deviation of the beam, either lateral or vertical. The position and the intensity of the reflected laser spot on the photodetector allow it to calculated these deflections. Therefore, this indicates the horizontal and vertical bending of the cantilever, allowing the AFM to measure the vertical and lateral deflection signals effectively.

Other mechanical elements such as:

a. Z motion motors which move the AFM scanner gently towards the sample.
b. AFM scanner to measure the force between the surface and the probe.
c. X-Y stage, which allows changing the sample position under the probe.

– A mechanical loop consists of all the mechanical components between the sample surface and the probe.
– Optical microscopy usually helps in the laser focusing beam at the beginning of each measurement process and provides a good visualization.
– An electronic feedback control circuit allows detecting the error and the noise signals, thus maintaining a good scanning and control of the data.
– A computer with suitable software to manage the measurement.

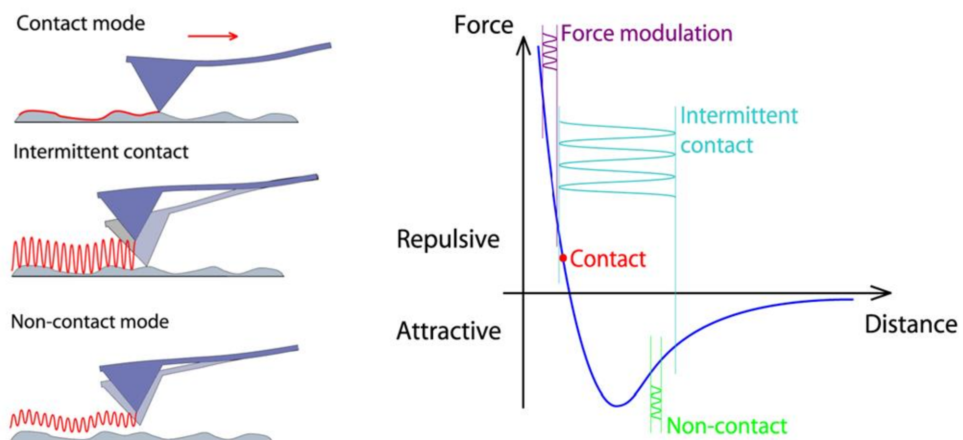

Fig. 20. The operation modes and their region in the force versus distance graph [51].

Mainly, there are three operation modes (**Fig. 17**).

1. Contact mode: in the following, the cantilever deflection is measured while the cantilever moves over the sample with an applied force. Here, considering that the higher parts of the surface will be exposed to a higher force, monitoring the cantilever height by a feedback loop is vital. This controlling is possible by selecting a range of deflection force. Consequently, the feedback system adjusts the cantilever height to maintain that the deflection obtained value does not exceed its selected range.

2. Dynamic modes, including intermittent contact and the non-contact modes. The first mode is a pretty used mode, where the tip does not touch the sample surface most of the time. When the probe touches the surface, a repulsive force is detected. However, in the second mode, the tip oscillates close to the sample without any contact. Moreover, this mode is not frequently utilized since contact with the sample surface is probably due to the attractive force. In both cases, the cantilever vibrates or oscillates on the sample, and this oscillation is measured instead of deflection. Usually, setpoint amplitude is selected, and the feedback system modifies the height to match this amplitude.
3. A new operation mode was recently developed by JPK instruments company called Quantitative Imagining or simply “QI.” In this case, the vertical force variates in each pixel as an algorithm regulates the tip movement to overcome the lateral forces and controls the vertical forces. On the other hand, this mode takes a long time to be performed, around 3.5 hours for each image, where is less than 25 min in the previous operation modes.

Methodology

Technically, the roughness measurement was performed utilizing AC mode or tapping mode and using the cantilever called "PPP-NchAuD" or "PointProbe" (Plus Non-Contact High Resonance Frequency - Au coating on the detector Side). While measuring the adhesion values, Quantitative Imaging or QI operation mode was adopted, and the process requested the same cantilever. However, to determine the friction, it was necessary to use a different cantilever labeled "CP-FM-PM-A" with 1,5 $\pm$ 10% μm the diameter of the ball on the tip, and contact mode was applied.

The technical properties of these cantilevers are given in **Table 3** [29] [31]. For each measurement operation, the JPK data processing software provides broad measurement parameters such as the height profile, vertical and lateral deflection, adhesion, and many other channels. Before engaging the measurement, several parameters could be selected as wanted in particular, the line rate (which is the speed of the cantilever on the x-axis), the x and y offsets, setpoint (the applied force on the cantilever), the size of the measured area as repesented in the appendix **Fig. 40**).

The SEM images for the probe on the top of each cantilever are shown in **Fig. 21**. On the left side of this picture, the cantilever named "PPP-NchAuD" is displayed. This cantilever is coated with a gold film on its top layer to enhance the intensity of the reflected laser light. Therefore, it can be easier for the photodetector to detect any minor light intensity changes. These measurements were done in the Otto Schott Institute for Materials Research in Jena city, Germany.

Table 3. Cantilevers technical data, Nominal values and specified ranges [29, 31, 52].

Property	Nominal Value			Specified Range		
	PPP-NchAuD	CP-FM-PM-A-1.5	ContAl-G	PPP-NchAuD	CP-FM-PM-A-1.5	ContAl-G
Resonance Frequency [kHz]	330	75	13	204 - 497	45 - 115	9 - 17
Force Constant [N/m]	42	2.8	0.2	10 - 130	0.5 - 9.5	0.07 - 0.4
Length [μm]	125	225	450	115- 135	$\pm$ 10 μm	$\pm$ 10
Mean Width [μm]	30	28	50	22.5 - 37.5	$\pm$ 7.5 μm	$\pm$ 5
Thickness [μm]	4	3	2	3 - 5	$\pm$ 1 μm	$\pm$ 1

3.2.1. Roughness

The main roughness amplitude parameters which were measured using JPK Data Processing software are average roughness (R_a), root mean square roughness (R_q), The Skewness (R_{sk}), and The Kurtosis (R_{ku}). These parameters can be defined as following [61]:

Ra: Average Roughness or arithmetical mean deviation is the average deviation of all points roughness profile from a mean line over the evaluation length.

$$R_a = \frac{1}{N} \sum_{j=1}^{N} |r_j| \quad (5)$$

R_q: Root Mean Square Roughness (RMS), is the average of the measured height variation,

$$R_q = \sqrt{\frac{1}{N} \sum_{j=1}^{N} r_j^2} \quad (6)$$

Rsk: The Skewness, it measures the symmetry of the height profile changing about its mean line.

$$R_{sk} = \frac{1}{NR_q^3} \sum_{j=1}^{N} r_j^3 \quad (7)$$

Rku: The Kurtosis, it presents the uniformity of the amplitude distribution function (ADF).

$$R_{ku} = \frac{1}{NR_q^4} \sum_{j=1}^{N} r_j^4 \quad (8)$$

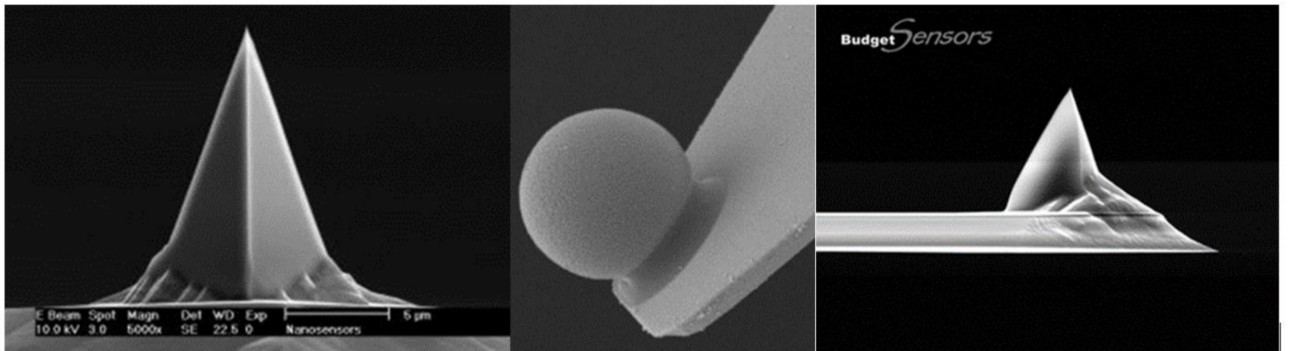

Fig. 21. SEM images of the three cantilevers types in the **Table 3**[29, 31, 52].

3.2.2. Fractal dimension and self-affinity

After getting the roughness parameters. The fractal dimension D_f and the self-affinity of the surface were investigated using the B N J Persson et al. methodology [60].

Generally, the surfaces such as those prepared by the depostion of sputtered particles, have almost a Gaussian distribution. This indicates that the root mean square height (R_q) should be equal to the height of the half width distribution. And the probability density function of the Gaussian height distribution can be written as following [60]:

$$P(h) = \frac{1}{\sqrt{2\pi}\, h_{rms}} \exp(-\frac{h^2}{2\, h_{rms}^2}) \quad (9)$$

As example, the **Fig. 22** gives a well illustration from the literature.

The autocorrelation function is given by [61]:

$$G(\tau_x, \tau_y) = \iint_{-\infty}^{+\infty} z_1 z_2 w(z_1, z_2, \tau_x, \tau_y) dz_1 dz_2 = \lim_{S\to\infty} \frac{1}{S} \iint_S \xi(x_1, y_1)\xi(x_1 + \tau_x, y_1 + \tau_y) dx_1 dy_1$$

where z_1 and z_2 are the values of heights at points (x_1, y_1), (x_2, y_2); furthermore, $\tau_x = x_1 - x_2$ and $\tau_y = y_1 - y_2$. The function w (z_1, z_2, τ_x, τ_y) represents the two-dimensional probability density of the random function ξ (x, y) and τ is the length between these two points. This ξ (x, y) is a random function that represents the height at a given point (x, y).

Technically, as the data given by the AFM are districted (for example, in the tapping mode, the cantilever touches the surface in few points, the distance between two consecutive points is Δx), additionally, the AFM measurement is performed faster on one axis than the other (the measurement on the x-axis is faster than the y axis). For these two reasons, the autocorrelation function can be then estimated as below [61]:

$$G(m) = G(m, 0) = \frac{1}{N(M-m)} \sum_{l=1}^{N} \sum_{k=1}^{M-m} z_{k+m,l+n} z_{k+l} \tag{10}$$

Where, $m = \tau_x/\Delta x$ and $n = \tau_y/\Delta y$. Usually, the one-dimensional autocorrelation function is well fitted with the Gaussian function, i.e., it can be given by the following relation:

$$G_x(m) = \sigma^2 \exp(-\tau_x^2/T^2) \tag{11}$$

where σ stands for the root mean square deviation of the heights and T for the autocorrelation length.

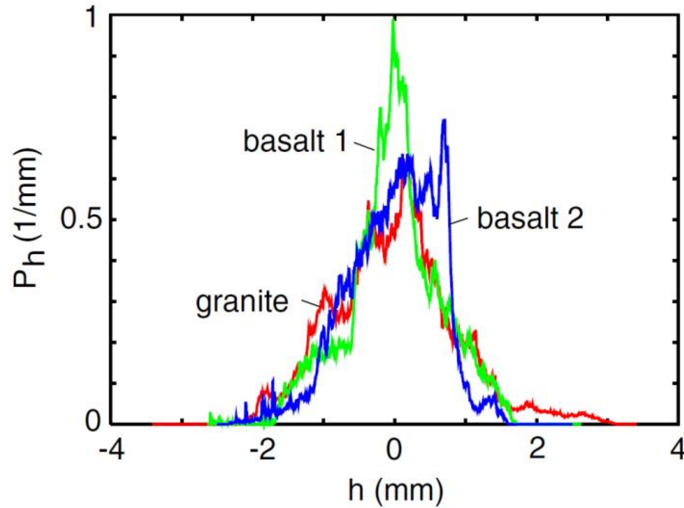

Fig. 22 . The height distribution graphs of different surfaces [60].

The adhesional and frictional properties are principally affected by the surface roughness power spectrum, the two-dimensional form of this function can be defined as the Fourier transform of the autocorrelation function mentioned previously, thus it can be written as below [61]:

$$W(K_x, K_y) = \frac{1}{4\pi} \iint_{-\infty}^{+\infty} G(\tau_x, \tau_y) e^{-i(K_x\tau_x + K_y\tau_y)} d\tau_x d\tau_y \tag{12}$$

Similarly, as described in the above section, this function can be written in the below form [60]:

$$C(q) = \frac{1}{(2\pi)^2} \int \langle h(x)h(0) \rangle \, e^{-iqx} \, d^2x \tag{13}$$

Here $\langle h(x) \rangle = 0$ represents a flat plane chosen as a reference and z = h(x) is the height of the surface at the point x = (x, y). The angular bracket $\langle ... \rangle$ indicates the ensemble averaging.

The corresponding Gaussian fitting relation for this function is [60]:

$$W_1(K_x) = \frac{\sigma^2 T}{2\sqrt{\pi}} \exp(-K_x^2 T^2/4) \tag{14}$$

Mostly, the surfaces which are interesting in this study domain are fractal self-affine surfaces [60]. Fractal is the property that allows the surface to looks the same when someone magnifies a section of it. In addition, self-affine means that the statistical properties (such as the height values distribution, variance, skewness, and kurtosis) are kept the same when changing the magnification scale. It was noticed that this property is valid when the magnification is performed on the parallel (on the XY plane) directions. However, on the perpendicular direction (z-direction), it is not applicable. Then, the power spectrum of a self-affine fractal surface is [60]:

$$C(q) \sim q^{-2(H+1)} \tag{15}$$

Where H is the Hurst exponent, and it is related to the fractal dimension D_f, via $D_f = 3-H$. Moreover, in reality the surfaces are not self-affine fractal overall length scales. As results, the wavevector is restricted between the highest possible value $q_1 \approx 2\,\pi/a$ and the smallest possible value $q_L \approx 2\,\pi/L$, where a and L are the lattice constant and the linear size of the surface, respectively. The **Fig. 23** provides an example.

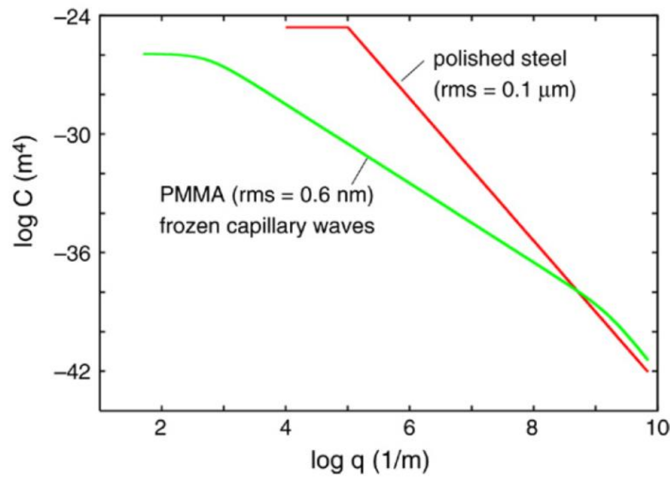

Fig. 23. The surface roughness power spectrum of two different roughness surfaces [60].

3.2.3. Adhesion

The adhesion value can be estimated as the difference in the vertical deflection value between the trace (or approach) and retrace for the stiff samples while changing versus the height of the surface. **Fig. 24** below illustrates an example from the AFM handbook [51].

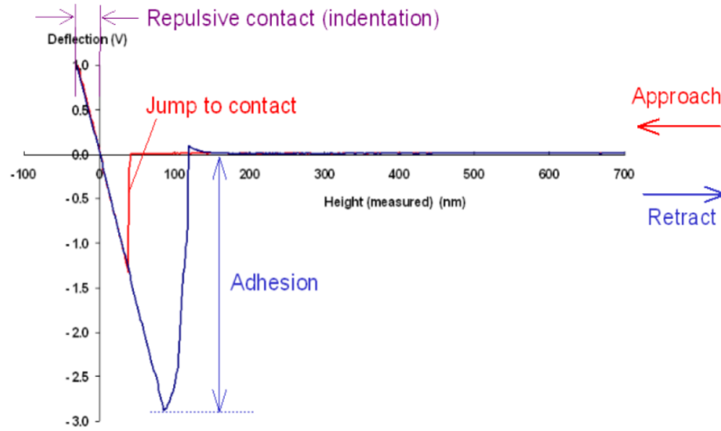

Fig. 24. The vertical deflection versus the height profile [51].

3.2.4. Friction measurements

During measuring using the sharp cantilever "ContAl-G", the applied normal force F_N leads to deflect this flexible cantilever. Meanwhile the surface scanner made by piezoelectric elements can detect and record the tip motion. Also, when the topography of the surface variates the applied F_N is controlled by a feedback loop. This bending of the cantilever can be measured from reflected laser light on the photodetector. The lateral force can be detected from signal measured by the four-quadrant photodetectors due to the spot laser displacement.

During measuring using the sharp cantilever "ContAl-G," the applied normal force F_N leads to deflect this flexible cantilever. Meanwhile, the surface scanner made by piezoelectric elements can detect and record the tip motion. Also, when the topography of the surface variates, the applied F_N is controlled by a feedback loop. The photodetector detects the reflected laser light and transforms it into a signal; thus, the electronic system uses it to compute the cantilever bending.

The lateral deflection signal is used to find the friction force values by analyzing the data in the latera deflection channels during the contact mode operation. It is necessary to consider the contribution of the surface topography, which can twist the cantilever, especially if artifacts existing on the surface, where a high torsion in the cantilever could occur. The lateral force images standardly are collected in both forward (retrace) and reverse (trace) directions to eliminate this issue. Therefore, the lateral signal in volt is calculated as it equals half of the difference between the trace retrace signals. After getting the mean value of the lateral force in volt, The cantilever calibration step needs some technical data to be known, similarly the cantilever dimension such as: the length (l), width (w), thickness (t), the tip height, density (ρ), Young's modulus (E) as well the shear modulus (G). Then (C_N) and (C_L), the normal and the lateral spring cantilever respectively. Finally, the lateral force in nN can be determined as follow [62]:

$$C_L = \frac{G\, W\, t^3}{3\, h^2\, l} \quad (15) \qquad C_N = \frac{E\, w\, t^3}{4\, l^3} \quad (16) \qquad F_L = \frac{3}{2} C_L \frac{h}{l} S_z V_L \quad (16)$$

Where, (S_z) is the photodetector sensitivity in nm/V. (V_L) is the lateral signal in V. Remark that the spring constant is strongly dependent on the cantilever thickness (t), and this last should be calculated using the formula below and not to be taken as its nominal value [62]:

$$t = \frac{2\pi\sqrt{12}}{1.875^2} \sqrt{\frac{\rho}{E}}\, f_0 l^2 \tag{17}$$

The thermal noise data file extracted from the AFM software contains the cantilever's oscillation frequency; the value of this frequency depends on the ambient conditions during the process. Extracting this parameter requires an additional step called "cantilever tune."; usually, this step is executed after the AFM laser and detector are aligned and before engaging the process.

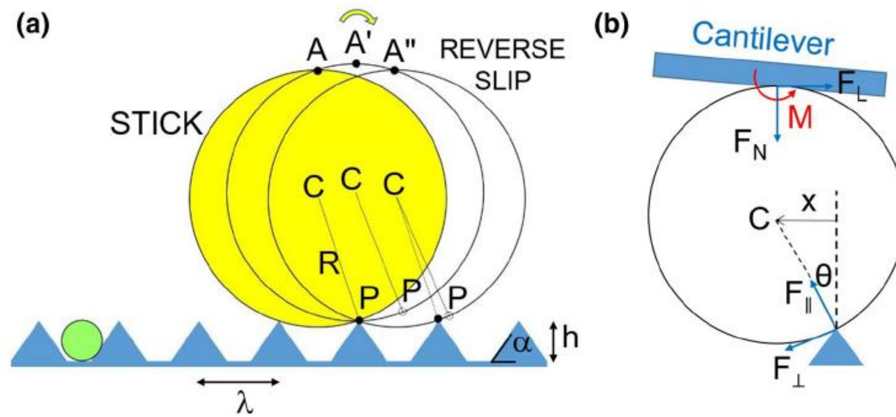

Fig. 25. The calibration method used, by Özoğul, A.[56].

In addition, by using the cantilever "PMMA-1.5" with 1.5 μm diameter of the ball on the tip. The calibration can be achieved using Ogletree's method (wedge method), or the method described in Özoğul, A. paper [56], where the cantilever was scanned over a commercially available reserve stick-slip the **Fig. 25**. This stick-slip has well-known morphology parameters which are provided from the manufacturers, and it is named SiO_2 grating (NT-MDT TGG1) with, periodicity λ = 3 μm, peak height h = 1.5 μm, alternated slopes α = ± 55° and edge radius < 10 nm as seen in **Fig. 25** In this paper, two different ball diameter was used 9.6 and 1.5 μm. The authors concluded that for the calibration of the smaller colloidal probes (r = 1.5 μm), Ogletree's method (wedge method), or the method described in this paper, can be used. However, for larger probes, Ogletree's method will not be feasible [56]. This paper determined that the lateral spring value was variated with the normal force applied during the measurement.

The results indicated a linear relationship between the friction and the normal force. Then the friction coefficient was determined (μ= 0.32). From the slop of the conflict versus the normal pressure. As the probe is made out of the polymer material, the study indicates the relation between the contact area (the contact area between this polymer probe and the sample) and the normal force applied [56]:

$$A_{con} = \frac{2F_N}{E^* \tan\alpha} \tag{18}$$

Where $E^* = E/(1-\nu)$, is the effective elastic modulus for PMMA. $E = 3.1$ MPa and $\nu = 0.35$. α, is an angle related to the material stiffness.

3.3. Raman Spectroscopy measurements

The theoretical function of this technique was described in section **2.2.**

The technical specification of the Raman spectroscopy used in this work measurements is included in **Table 4** below and the spectroscopy photo. The measurement parameters were selected as follows: exposure time 10 s, accumulations 3, laser power 0,3 mW, range from 100-2000 cm^{-1}, spot size ~10 μm. The measurement was done several times on different spots for each sample. The measurements were performed in Center for Hydrogen Energy Technologies, Lithuanian Energy Institute.

Table 4. The technical data of the Raman spectroscopy.

Excitation wavelength	Semiconductor laser power	Stokes lines range	Resolution
532 nm	45 mW	100 to 8000 cm^{-1}	< 1 cm^{-1}

Fig. 26. The Raman spectroscopy photo (Renishaw in Via Spectrometer with accessories) used in National innovation and entrepreneurship center in KTU.

There Raman data files were used to plot the Raman graphs. The D and G peaks were fitted with the Gaussian function with the aid of Origin software. Then, the statistical parameter was extracted such as the G peak position, the D peak position, the G peak full width at half maximum (FWHM), the ratio of the intensity peaks I(D)/(G), and their area ratio (A_D/A_G).

3.4. IR-visible-UV spectrophotometer

In definition, the spectrophotometer is a well-known scientific instrument used to investigate the amount of light absorbed by the measured samples or its light transmittance. One of the spectrophotometer's components is a lamp, which provides the light source. This light should have the same wavelength range intended to be used in the investigation. Then the beam of light hits a diffraction grating, which acts as a prism to split the light beam each wavelength in different directions following Bragg's law of light diffraction. Consequently, each beam can be focused and delivered toward the sample individually. This instrument has an exit slit, which allows each wavelength range to be pass-through alone, depending on the instrument's resolution. Also, it has a

detector located behind the sample that provides the signal intensity according to the power of the light, which transmitted or entirely passed through the object following the light Beer's law. The intensity difference between the incident beam and the transmitted one would refer to the absorbed light intensity.

In this research, the IR-visible-UV spectrophotometer "Ocean optics 4000" was used to measure the light transmittance of the thin films deposited on the glass with the same deposition parameters for those deposited on the silicon substrates. In the begging, it is necessary to measure the glass used without coating to measure the transmittance of the glass alone. The IR-visible-UV spectrophotometer “Ocean optics 4000” was used to measure the light transmittance of the thin films deposited on the glass with the same deposition parameters for those deposited on the silicon substrates. At the begging it is necessary to measure the glass used without coating in order to measure the transmittance the glass alone.

3.5. Energy Dispersive X-Ray Spectroscopy

Energy-dispersive X-ray spectroscopy (EDS) is a unique technique for an electron microscope. X-rays are generated due to interaction between the incident electrons and the atoms of the samples that get ionized. This technique is the acquisition and characterization of these X-rays. A modern version of EDS would consist of these three components, (1) the X-ray detector, a Silicon Drift Detector (SDD) to detect these X-rays and convert the data to an electronic signal. (2) a pulse processor which measures these electronic signals and calculates the energy of these detected X-rays. (3) Then, an analyzer displays an acquired spectrum by decomposing the overlap peaks and removing the background and noise.

In this work, the Bruker Quad 5040 spectrometer, AXS Microanalysis GmbH XPS, was used to measure the thin film's elemental composition. The measurement was done using the following parameters: 15 kV, surface area of ~1.15 mm^2, 3-5 different spots. The measurements were done in Center for Hydrogen Energy Technologies, Lithuanian Energy Institute.

4. Results and discussion

4.1. Surfaces morphology (AFM)

The height profile was measured at four different scales 1*1, 2.5*2.5, 5*5, and 10*10 μm^2; however, the values in **Table 5** were extracted from the scale 1*1 as it has the highest resolution.

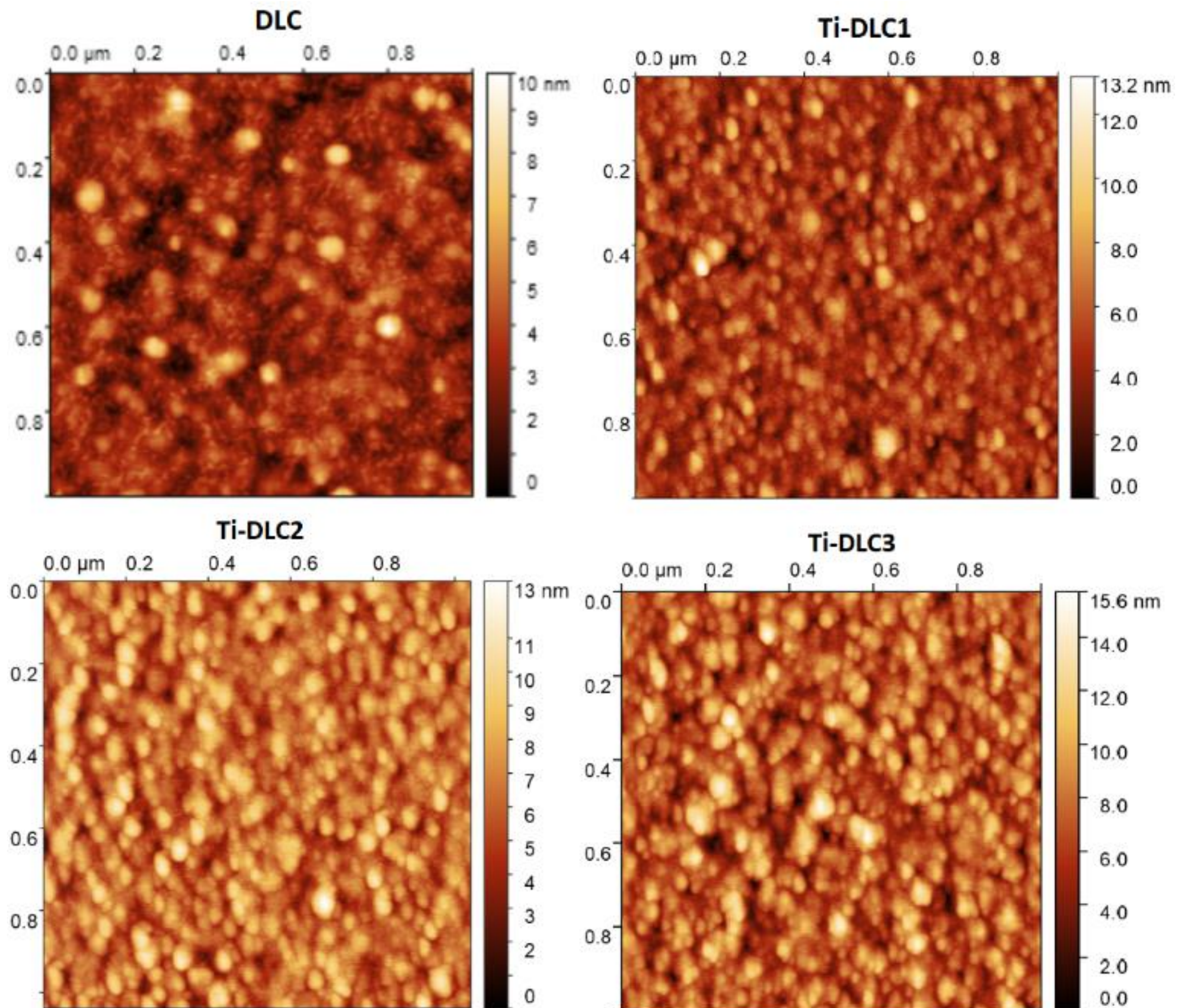

Fig. 27. Topography surface of the films.

Fig. 27 illustrates the topography of each sample. The existing small artifact can be seen. The light-colored spots on the surface representing the highest places on the surface. During the measurements, the artifacts can be avoided by scan a different area on the surface.

Table 5. The roughness parameters, Skewness and Kurtosis, as well the Hurst component H and the fractal dimension D_f of each sample.

Sample code	R_a [nm]	R_q (RMS) [nm]	R_{sk}	R_{ku}	H	D_f
DLC	0.86 ± 0.11	1.15 ± 0.19	0.84 ± 0.54	1.61 ± 2.16	0.87	2.19
Ti-DLC1	1.06 ± 0.16	1.37 ± 0.23	0.41 ± 0.44	0.42 ± 1.06	0.17	2.83
Ti-DLC2	1.4 ± 0.10	1.82 ± 0.12	0.45 ± 0.21	0.35 ± 0.63	0.22	2.79
Ti-DLC3	1.68 ± 0.24	2.13 ± 0.29	0.25 ± 0.29	−0.06 ± 0.43	0.35	2.65

In **Table 5**, the statistical quantities of the roughness parameters were extracted from the images with the scale (1 µm * 1µm). The surface roughness was the lowest for the DLC films. The R_a and R_q values were 0.86 nm and 1.15 nm, respectively (**Fig. 28**). The roughness was slightly increased from 1.37 nm to 2.13 nm with the increase of the Ti concentration from 4.5 at. % to 23 at. %. Likewise, here [27], the RMS value decreased from 6.50 nm to 0.68 nm with the decrement in the Ti amount from 30.3 at. % to 4.5 at. %. In this research [33], the rise was from 5.027 nm to 9.181 nm at 0% and 5.8 at. % Ti. It is noticed that in this previous study, the sp^2/sp^3 ratio incremented from 1.1 to 2.1. Also, this ratio varied from 1.58 to 5.5 in this paper [27]. Thus, the amorphization of the films acts to increase the roughness. Similar trends for the chromium metal were observed by J.A. Santiago [69], where the increase was from 4.7 to 6.2 nm with Cr content from 0 at. % up to 20 at. %. Thus, the addition of metal dopants enhances the surface roughness of the doped DLC due to the formation of larger size particles.

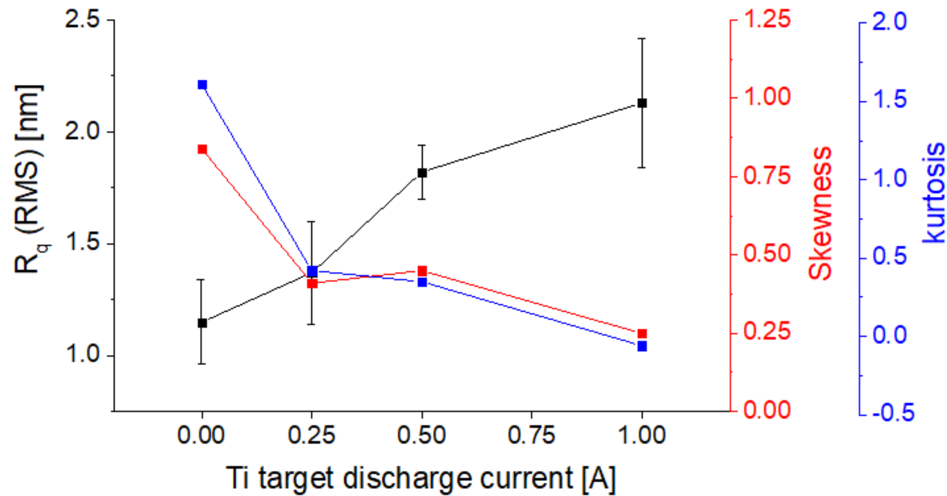

Fig. 28. The root mean squared roughness R_q, skwevness and kurtosis versus the Ti target discharge current.

Meanwhile, the skewness and the kurtosis were decreased; however, the authors rarely investigated these parameters in the literature. Using the J Robertson theory [60], it is possible to check the self-affinity of the samples, where the fractal dimension D_f was calculated as described in section **3.2.1,** according to this theory, the surface is self-affine if $2 < D_f < 3$; and this is what was observed in **Table 5**. The meaning and the equation of the skewness (R_{sk}) and the kurtosis (R_{ku}) are given in section **3.2.1**. The skewness and kurtosis values for the DLC film were 0.84 and 1.61, respectively (**Fig. 28**). The trend of these parameters with the addition of Ti is shown in **Fig. 28**, where the decrease was from 0.84 to 0.25 and from 1.61 to -0.06 for skewness and kurtosis, respectively.

It should be noted that the films formed at Ti discharge currents of 0.25 and 0.50 A had similar skewness values (**Table 5**). The positive values of the skewness indicate the domination of the peaks on the surface for films, and as the highest value is much less than three; thus, these results indicate a low number of high peaks and low valleys. In conclusion, the profile is homogenous, and coating is homogeneously distributed and does not form large specks. A similar analysis was provided by M. Černauskas et al. [68] to deposition nanostructured amorphous carbon-copper composite films.Elemental composition of the films.

Table 6 below constitutes the average values of the elemental composition of each sample using the EDS technique. The experimental details were provided previously in section **3.5**. The average values of the elemental atomic are given in **Table 7**, except the silicon element as the substrate is made out

of silicon; hence, these values were renormalized. These values would be merely the elemental atomic of the deposited coating, considering that during the deposition, the temperature was too low (In the begging it was at room temperature, then it reached ~150 ^{0}C during the process) to initiate any diffusion of the silicon ions from the substrate into the coated films. Also, in this table, the error was calculated using the variance definition.

Table 6. The average values of the elemental weight and atomic percentage of each sample.

Sample \ Element	Silicon		Carbon		Oxygen		Titanium	
	wt. %	at. %	wt. %	at. %	wt. %	at. %	wt. %	at. %
DLC	74.9	57.2	22.6	39.4	2.5	3.4	0	0
Ti-DLC1	73.7	59.1	15.5	29.3	6.9	9.7	3.9	1.9
Ti-DLC2	64.8	52.6	14.2	26.9	11.0	15.7	10.0	4.8
Ti-DLC3	44.8	37.9	17.2	34.0	9.40	13.9	28.6	14.1

The graph in **Fig. 29** reveals the variation of these atomic elemental compositions of DLC films versus the titanium target discharge current. In the range between 0 and 0.5 A, the carbon content decreased from 92.1 at. % to 56.8 at. %. Contrarily and as excepted, the titanium content increased from 0 at. % to 10.1 at. %. Similarly, the oxygen content shifted from 7.9 at. % to 33.1 at. %. The trend of titanium content was expected as the increase of discharge current will enhance the plasma. Thus more Ti ions will be deposited. The oxygen amount increasing is due to the high reactivity of the titanium with the oxygen. This increase indicates the formation of titanium oxide in the sample [27]. The reason for having this high oxygen amount is that before the coating beginning, the sputter-cleaning of the titanium target was done. Therefore, during the cleaning process, some of the oxygen residues in the chamber were united with the titanium target before deposited on the films.

Table 7. The average values of the elemental atomic concentration renormalized without the silicon element.

Samples	Carbon at.%	Oxygen at.%	Titanium at.%
DLC	92.1 ± 0.5	7.9 ± 0.5	0
Ti-DLC1	71.7 ± 0.2	23.8 ± 0.2	4.5 ± 0.1
Ti-DLC2	56.8 ± 0.2	33.1 ± 0.3	10.1 ± 0.2
Ti-DLC3	54.7± 0.8	22.4 ± 0.3	22.9 ± 0.7

For further increase in the titanium discharge current until 1.00 A, it was noticed that the oxygen content started to decrease with the increase in the titanium content until 22.4 at. % of O. However, the Ti content continues in the elevation until ~23 at. % of Ti (**Fig. 29**). These trends could indicate the formation of the Ti carbide and reduction in the titanium oxide in the coating. As observed here [28], the cubic TiC nanocrystalline clusters were embedded in the structure at 5.3 at. % Ti, however, in this study, the oxygen amount was about 1.7 at. % much lower than 22.4 at. %. The reason for obtaining a high amount of oxygen could be due to the high difference in electronegativities between oxygen (3.44) and titanium (1.54). As the electronegativity of the Ti is the lowest 1.54, the formation of titanium oxides is predictable when the Ti atoms are sputtered. Likewise, the formation of the C-O or C=O bonds is more favorite comparing to C-Ti. S. Zhang et al. [70] indicate that doping with a low amount of Ti (between 1 and 2 at. %) leads to an increase in the oxygen amount between 8 at. %

to 11 at. %. N.W. Khun et al. [71] and J.A. Santiago [69] and L. Sun [72] found similar results utilizing other dopant metals such as nickel and chromium. It was proved that the addition of the Cr into DLC films causes the formation of several chemical bonds such as Cr-C, Cr_2O_3, or $Cr(OH)_3$. Also, the formation of the C-O or C=O bonds is faster than metal oxides with the increase of thte metal concentration. For further investigation of bonding type in the films, the XPS investigation should be performed.

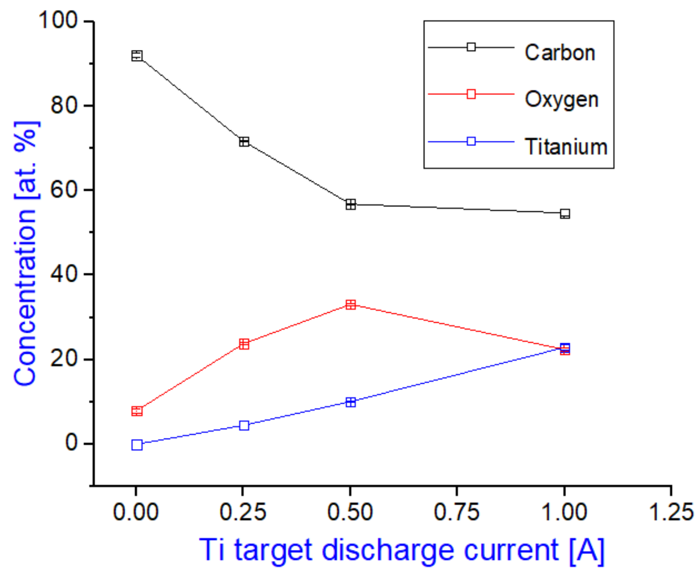

Fig. 29. The elemental atomic percentage versus the Ti target discharge current.

4.2. Light transmittance

The graph in **Fig. 30** provides the variation of the light transmittance measured by the IR-visible-UV spectrophotometer for the coating deposited on glass substrates. The transmittance values dramatically increased with the increase of the wavelength for the whole samples except for the Ti-DLC3 it was slightly increased. For the Ti-DLC3 sample and contrarily to the others, the transmittance percentage was much lower at the whole measured range of wavelengths (**Fig. 30**). The highest transmittance value at 890 nm was for DLC coating (~50 %) and the lowest for Ti-DLC3 (~8.5%). Such type of measurement was mainly not performed in the literature. In detail, the light transmittance was proportionally increased with the increase of the wavelength from 365 nm to 890 nm. For the DLC, Ti-DLC1, and Ti-DLC2 films, it starts from ~1.5 % at ~365 nm then increased to ~40% for Ti-doped films, while it reached a higher value with 50% for the DLC one; all at ~890 nm. However, in the Ti-DLC3 case, the increase of transmittance from ~0.1 % to ~8.5% was observed.

As known, the thickness of the coating influences the light transmittance values. The thickness was not measured in this work, but it is known from measurement on a similar coating that the thickness is about 250 nm for the DLC and Ti-DLC1. Meanwhile the thickness of the Ti-DLC3 was the highest, according to the EDS results. Moreover, the coating is uniform distributed on the surface. Thus, it could be concluded that the Ti content with ~23% in the DLC coating attenuates most of the light between 360 and 890 nm. Previously, B. Zhou [73] demonstrated that the optical transmittance of the DLC films decreased with the increase of the Cu amount. Furthermore, Pandey et al. [74] found that the increase in the nickel content causes the reduction in the transmission from 85 % to 35 %.

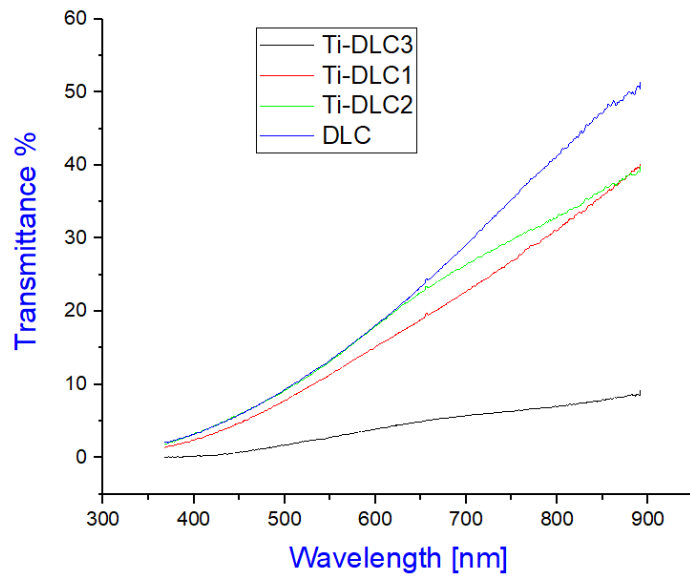

Fig. 30. The light transmittance of the samples.

4.3. Raman spectra

In **Fig. 31** below, the Raman spectra of the doped DLC films are plotted in one graph using Origin software. This graph illustrates how the intensity was reduced with the increase of the titanium content in the film, which was observed by D. Savchenko et al. [64].

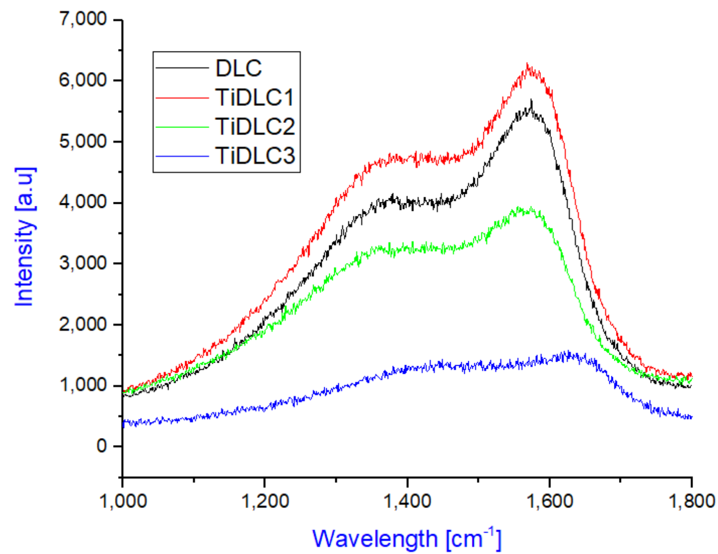

Fig. 31. The Raman spectra of the samples between 1000 and 1800 cm^{-1} wavelength.

The measurement parameters were selected as mentioned in section **3.3**. In **Fig. 31**, the spectra are shown between 1000 and 1800 cm-1; in this range, the G and D peaks appear.

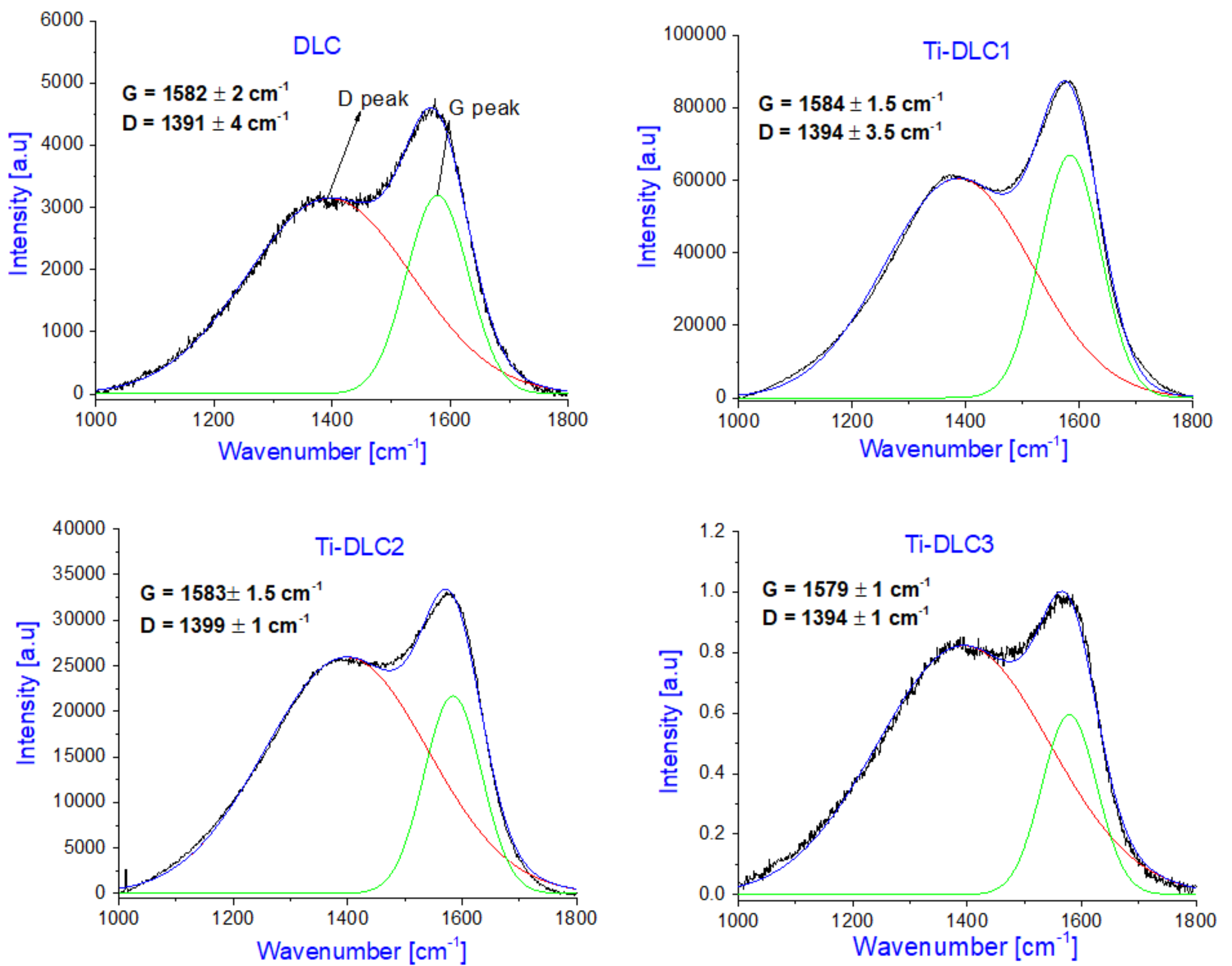

Fig. 32. The Raman spectra of each sample fitted with Gaussian function. The average spectra parameters were included in the graph of each sample.

In **Fig. 32**, the Raman spectra were well fitted with the Gaussian function. This step has to be done in order to extract the Raman parameters, which are included in the graph of each sample. The D and G peaks were illustrated in the graph (D in red and G in Green). In **Fig. 33**, when the Ti target discharge current was increased from 0 to 1.00 A. The intensity peak ratio I(D)/I(G) was increased from 0.96 to 1.39, and the G peak full width at half maximum (FWHM) becomes narrower from 125 to 115 cm^{-1}, in the same range of Ti changing. These two parameter trends are well fitted with the results of other studies. Similar trends were observed with using of different metals, especially in the chromium case. Also, this study indicates that the increase in the I(D)/I(G) demonstrates a higher disorder in the coating, more aromatic disorder rings, or increasing in the sp^2 carbon sites [64]. As well, many other authors obtained a similar trend [30, 32, 35, 65].

However, regarding the G peak position, it can be noticed that the G peak position shifted to a higher position from ~1581 cm^{-1} to ~1583 cm^{-1} in the first increase of the Ti target discharge current till 0.25 A before shifting to a lower position (1579 cm^{-1} at 1.00 A). Considering the error bars, the G position was almost stable. This trend differs from the trends for most studies in the bibliography [15, 32, 34, 35]. The reason for having this trend could be due to the oxygen amount, and this is what was proving the W. Liu et al. [27] study, where a similar trend was noticed, and the G peak position increased from 1544 cm^{-1} to 1557 cm^{-1} before reduced to 1549 cm^{-1}. Additionally, A.M. Qasim et al. [75]

demonstrated that oxygen's introduction leads to modifying the coating's structure. Also, a large amount of oxygen causes the sp^2/sp^3 ratio to be increased radically and heightens the presence of carboxyl (O–C=O) groups and carbonyl (C=O) groups. M. Evaristo et al. [76] found that the oxygen existence responsible for augmenting graphitic clusters and the sp^2 content. Moreover, the trend of other parameters such as the intensity peak ratio A(D)/A(G) and the D peak position could be used to analyze the Raman spectra' data. The D peak shifted from 1391 cm^{-1} to 1399 cm^{-1}, when the Ti concentration increased from 0 at. % to 10.1 at. % (**Fig. 32**). Meanwhile, the position of the D peak was slightly reduced to 1394 cm^{-1} at the highest Ti concentration. In this work, the A(D)/A(G) ratio raised from 2.62 to 4.33 with the increase of Ti content, and this result agreed with the previously mentioned studies. Thus, the Raman results indicated that the addition of Ti (and increase of oxygen) stipulate the formation of films with a higher fraction of sp^2 sites.

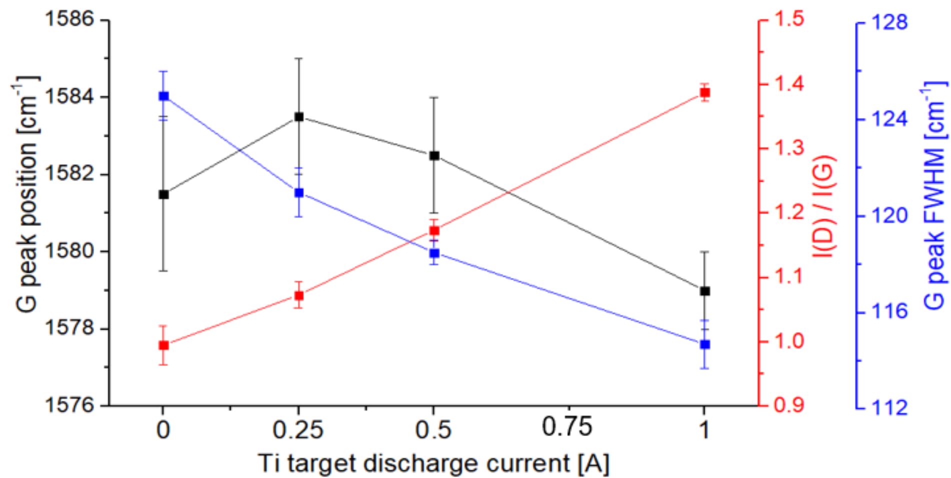

Fig. 33. The Raman spectra main parameters variation versus the Ti discharge current.

4.4. Adhesion (AFM)

Each sample's adhesion measurement was done on three different scales (1*1, 2.5*2.5, and 10μm*10μm). **Fig. 34** represents the adhesion measurement at the scale of 1 μm * 1 μm. The data of the images were extracted from JPK data processing software and not from the Gwyddion software, as this last is not compatible with this new operation mode. The single image file has ~5 GB size as it has the adhesion graph illustrated in **Fig. 24** for every single pixel (there are 512*512 pixels in each image). The values in **Table 8** represent the average out of the three scales. The adhesion value was proportionally decreased (from ~14 nN to ~6 nN) as the Ti discharge current increased from 0 to 1.00 A. This QI operation mode took a long time to be done for each image (~3.5 hours, where it is less than half-hour for the other operation modes). In the mentioned table, adhesion, setpoint, and measured slope average values are included.

Table 8. The samples adhesion parameters values from the Quantitative Imaging operation mode data.

Samples	Adhesion [nN]	Setpoint [nN]	Measured slope [N/m]
DLC	13.98	64.57	17.99
Ti-DLC1	9.72	71.94	22.65
Ti-DLC2	8.81	71.94	17.08
Ti-DLC3	5.99	70.40	21.77

The setpoint was changed depending on the surface morphology at each pixel following a specific algorithm. In the literature, most of the investigation is about the coating adhesion itself, where nanoindentation and scratch test was used [30, 35, 36].

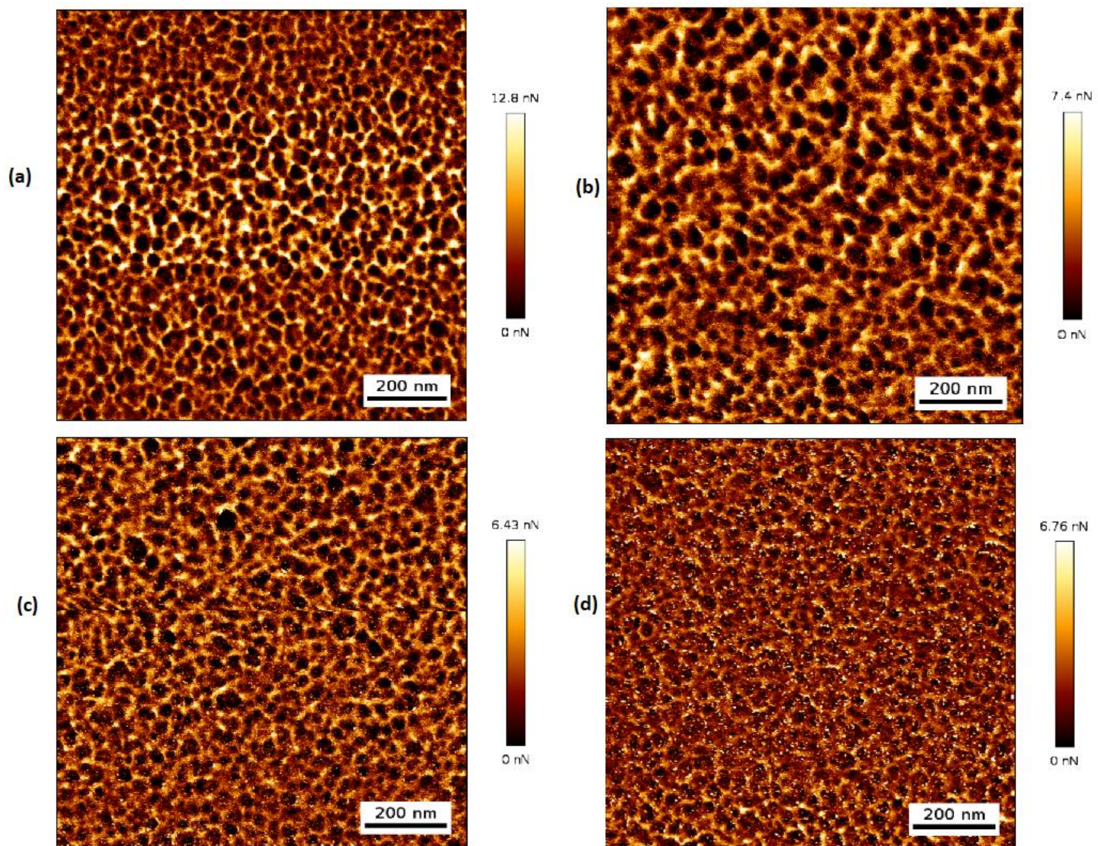

Fig. 34. The adhesion figures of (a) DLC, (b) Ti-DLC1, (c) Ti-DLC2, (d) Ti-DLC3 films.

Generally, it was demonstrated that the increase of the metal concentration in DLC films decreased the contact angles [66], which indicates an increase in the surface energy, and thus the adhesion will be lower. Also, the doping of the DLC films with oxygen caused to increase in wettability [67].

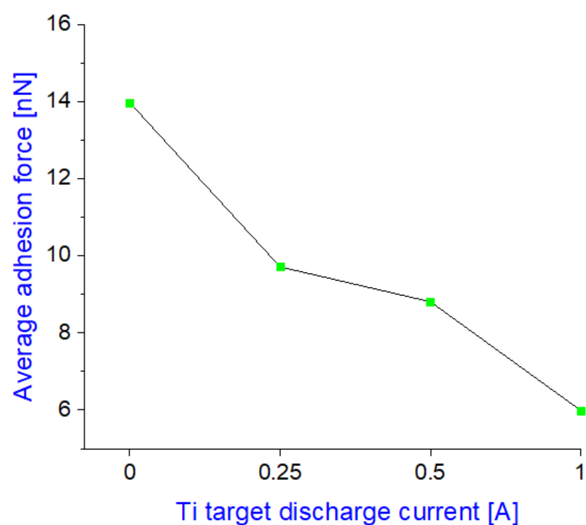

Fig. 35. The average adhesion values of each sample

4.5. Friction using “ContAl-G” cantilever (AFM)

Generally, the AFM provides the lateral deflection signal in Volt. **Fig. 36** illustrates the lateral deflection channels trace and retrace of the sample Ti-DLC2 at 80 nN normal force applied on the sharp “ConAl-G” cantilever. “trace” means when the cantilever. Scan one line of the surface from right to left and “retrace” in the opposite direction for the same line. It is regarded how the lateral values in the retrace channels have a higher value than the trace one.

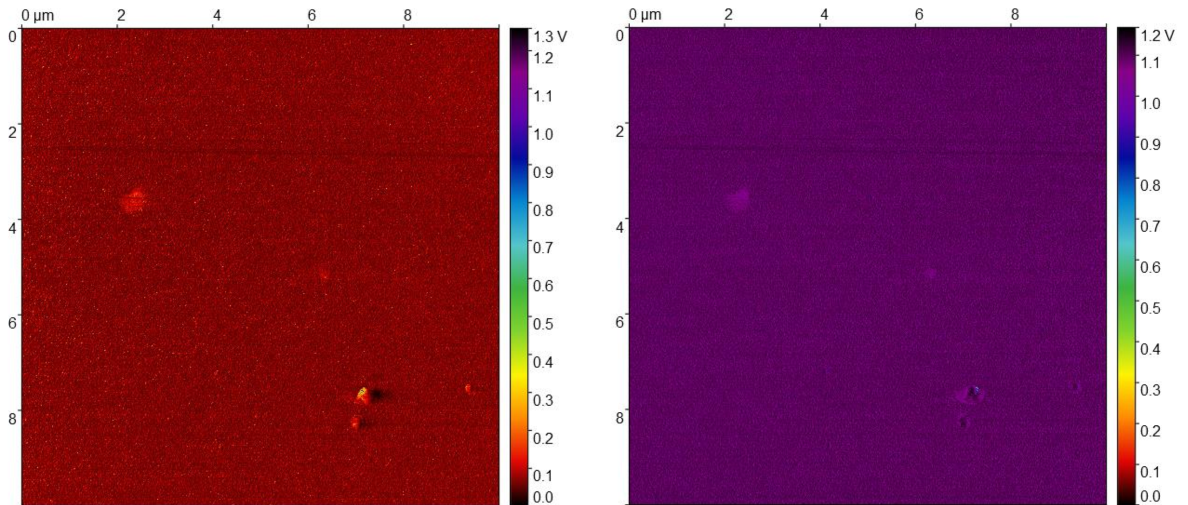

Fig. 36. The lateral deflection of the sample Ti-DLC2 at 80nN set point, from the right, trace and retrace channels.

Normal force [nN]	Friction force [nN]			
	DLC	Ti-DLC1	Ti-DLC2	Ti-DLC3
10.0	21.1	23.0	110.7	19.7
20.0	97.4	38.7	34.7	48.5
30.0	52.3	25.3	122.6	47.1
40.0	36.6	67.7	113.2	47.8
50.0	30.3	49.7	173.4	60.9
60.0	37.8	26.1	100.1	54.3
70.0	33.6	34.2	87.7	65.5
80.0	42.5	14.0	193.1	61.6
90.0	38.6	21.8	---	59.9

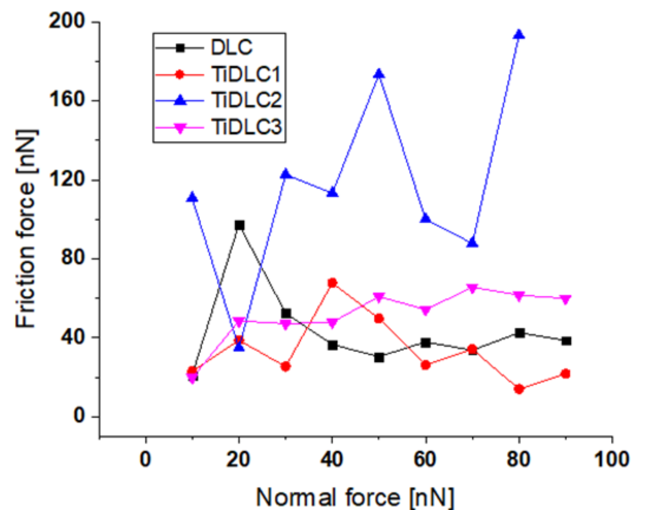

Fig. 37. On the left the friction values at each normal force. And on the right the graph of the friction force versus the normal force measured using the sharp cantilever “ContAl-G”.

The presence of one artifact is noticed in these images (on the top-down part, a shape appears on the image, and it has a high value). These artifacts highly modified the average value of the lateral signal in V extracted for each image. So, it is necessary to avoid them using the "Multiprofile" tool in the "Gwyddion" software; this tool allows the user to choose the lines on the surface selectively.

Fig. 37 shows the values of the friction force, the method used in the calculation was previously described in section **3.2.4**. In this figure's graph, the friction values fluctuated as the normal force

increased from 10 to 90 nN. This range of normal force was chosen as recommended in the user manual of this cantilever. (depending on the stiffness of the sample material. The choice of higher values usually leads to either damaging the sample or break the cantilever).

In this work, between 14 nN at 80 nN applied force on the cantilever, the whole samples' friction forces fluctuated with the increment of the applied force, mostly the Ti-DLC2. The DLC sample had a fluctuated friction force between ~21 nN and ~98 nN; for Ti-DLC1, this value was between ~22 nN and ~68 nN; for Ti-DLC2, it was the highest between ~35 nN and ~193 nN; for Ti-DLC3 it was between ~20 nN and ~66 nN.

It was noticed that the lowest friction value of ~14 nN at 80 nN normal force was recorded for the Ti-DLC1 sample, corresponding to a friction coefficient value of μ 0.175. While the highest value of ~194 nN was measured for the sample Ti-DLC2 at 80 nN. Similar behavior was found (the friction coefficient of 0.13 was obtained between 6 and 8% [36, 32, 15]). However, mainly the authors utilized different techniques to investigate the friction coefficient, such as the ball on the disc instrument.

4.6. Friction using "PMMA-1.5" cantilever (AFM)

The lateral deflection channels trace and retrace at 25 nN applied normal force of the "PMMA" cantilever are provided in **Fig. 38**. It can be seen the rounded shape of the probe in both images. However, for most samples and at different applied forces, their scanned images had weird horizontal lines. Even with cleaning the samples and changing the feedback and setpoint parameters, these lines did not disappear. The results could indicate that the probe was sliding on the surface, which distorted the images. The cutting tool was used to overcome this issue.

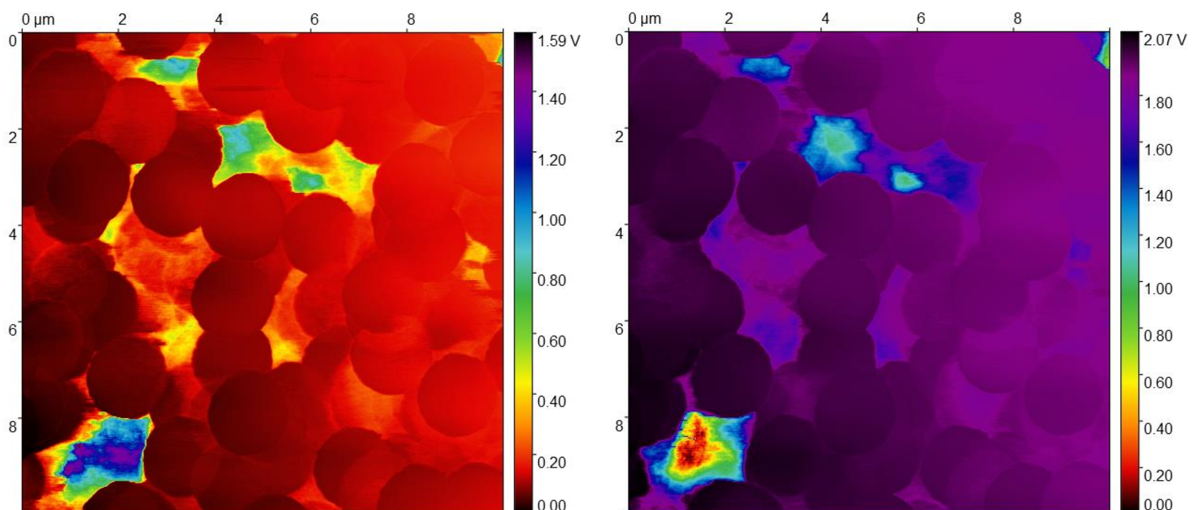

Fig. 38. The lateral deflection of the sample at 25nN set point, from the right, trace and retrace channels.

Fig. 39 includes the table of the friction force for each sample versus the applied normal force. After getting the lateral deflection signals in volt, the cantilever must be calibrated using one of the methods mentioned in section **3.2.4**. Unfortunately, in this work, this step was not accomplished. The graph below shows the lateral deflection variation in volt with the regular force in nN.

In the range from 25 to 150 nN for the applied force, the lateral deflection signal decreased from 0.918 to 0.788 V before reincreasing until 0.967 V for the DLC sample. While for Ti-DLC2, it

increased from 1.09 to 1.193 V. However, for the Ti-DLC2, the fluctuation was evident. The change was between 0.606 and 0.776 V. The Ti-DLC3 sample had the lowest lateral deflection signal with a slight variation between 0.408 and 0.459 V in the normal force range of 25-150 nN (**Fig. 39**).

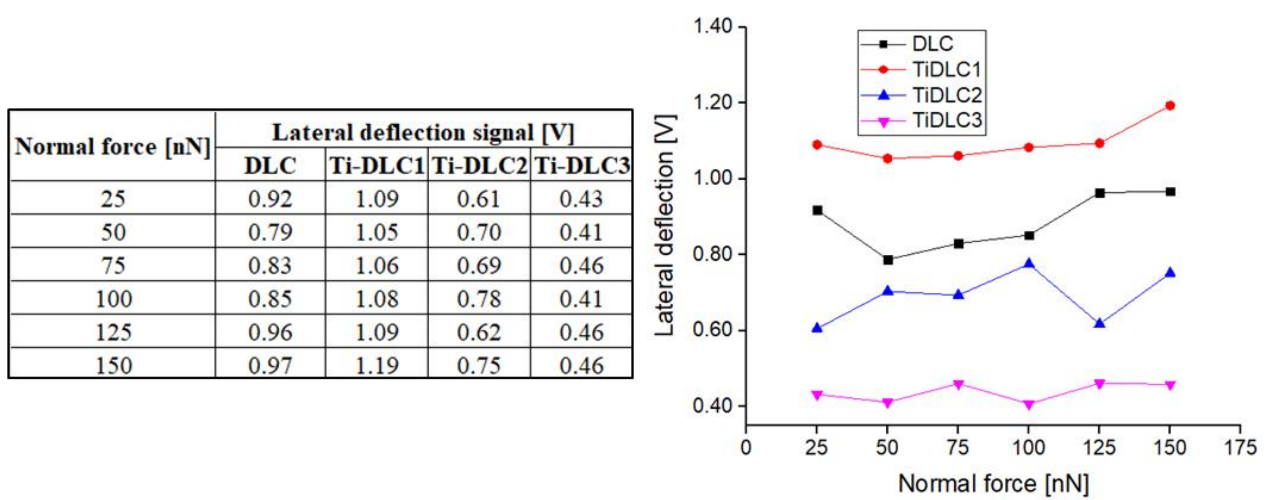

Normal force [nN]	Lateral deflection signal [V]			
	DLC	Ti-DLC1	Ti-DLC2	Ti-DLC3
25	0.92	1.09	0.61	0.43
50	0.79	1.05	0.70	0.41
75	0.83	1.06	0.69	0.46
100	0.85	1.08	0.78	0.41
125	0.96	1.09	0.62	0.46
150	0.97	1.19	0.75	0.46

Fig. 39. The lateral deflection signal in volt for each samples versus the normal force in nN

The lateral deflection signals values were stable, and the Ti-DLC3 (with Ti target discharge current 1.00 A) showed the lowest friction. This paper [56] indicated that the friction coefficient slightly changed in this range of applied force values. Also, it revealed that conversion value C in nN/V rises with the increment of the normal force, where the conversion value slightly increased between ~220 and ~290. In this project, a calibration of the value in this work is vital to compare with other studies.

Conclusions

1. The elemental composition measurements indicated the increase of the titanium concentration in the DLC films from 4.5 at. % to 22.9 at. % with the Ti target discharges current from 0.25 A to 1.00 A increment.
2. The Raman spectroscopy measurements demonstrated that the doped DLC films contained a high fraction of sp^2 carbon sites. The sp^2/sp^3 carbon sites ratio (graphitization) in the films increased with Ti concentrations.
3. The highest transparency values in the range between 360-900 nm were for the DLC film without Ti. The transmittance of the Ti-doped DLC films was reduced with the increase of the Ti content.
4. The surface roughness of the films slightly increased from 0.9 nm to 1.7 nm. The adhesion decreased from 14 nN to 6 nN, while skewness and kurtosis parameters were reduced with Ti concentration. The results indicated that the surfaces of the films have a self-affine shape.
5. The friction force measured using the sharp cantilever has fluctuated (topography contribution). The DLC film with the lowest Ti concentration showed the lowest friction force of ~14 nN at 80 nN normal force (μ ~0.175).
6. The lateral deflection signal values measured using the "PMMA-1.5 μm of diameter" cantilever show much stability with the applied normal force variation between 20 and 100 nN. The lowest lateral deflection signal is recorded for the Ti-DLC3 film with ~23 at. % of Ti, due to the highest sp^2 sites fraction.

Acknowledgement

The Traineeship opportunity I had at Otto Schott Institute for Materials Research was a great chance to learn about the AFM, especially from a technical perspective. Therefore, I would like to express my deepest gratitude and special thanks to Prof. Enrico Gnecco, who, despite having many works, provides well guide, tried to keep me on the correct path. I would also like to express my deepest thanks to my thesis supervisor, Professor Liutauras Marcinauskas, for providing me this chance and for his help to improve this work continuously. Similarly, I also want to thank Ph.D. student Vilius Dovydaitis, who provided the Raman spectroscopy and EDS data.

Participation in conferences

I would like to declare that part of the results in this work was presented at this conference:

Hassan, Zhairabany*; Liutauras, Marcinauskas; Vilius, Dovydaitis; Enrico, Gnecco. Mathematics and Natural Sciences // Theory and Application: Kaunas, Lithuania, 6 May 2021 / organized by Kaunas University of Technology.

Likewise, some of the results will be exhibited by Vilius Dovydaitis in this upcoming conference:

Vilius, Dovydaitis*; Hassan, Zhairabany; Liutauras, Marcinauskas; Enrico, Gnecco; Paola, Ayala. Advanced Nano Materials ANM2020 // 17th International conference on Advanced Nanomaterials: Aveiro, Portugal, 22-24 July 2021 / organized by the University of Aveiro.

List of references

1. Prakasam M, Locs J, Salma-Ancane K, Loca D, Largeteau A, Berzina-Cimdina L. Biodegradable Materials and Metallic Implants-A Review. J Funct Biomater. 2017 Sep 26;8(4):44. doi: 10.3390/jfb8040044. PMID: 28954399; PMCID: PMC5748551.
2. Ferrari, A. C., Raman spectroscopy of graphene and graphite: Disorder, electronphonon coupling, doping and nonadiabatic effects. Solid State Communications 2007, 143 (12), 47-57.
3. V.-M. Tiainen: 'Amorphous carbon as a bio-mechanical coating – mechanical properties and biological applications', Diam. Relat. Mater., 2001, 10, (2), 153–160.
4. R. J. Narayan: 'Laser processing of diamond like carbon thin films for medical prostheses', Int. Mater. Rev., 2006, 51, (2), 127–143.
5. W MA, A J RUYS, H ZREIQAT, 16 - Diamond-like carbon (DLC) as a biocompatible coating in orthopaedic and cardiac medicine, Editor(s): Lucy Di Silvio, In Woodhead Publishing Series in Biomaterials, Cellular Response to Biomaterials, Woodhead
6. L. Schaefer et al.: 'Tribological applications of amorphous carbon and crystalline diamond coatings', Proc. 43rd SVC Ann. Techn. Conf., Denver, KL, USA, April 2000, Soceity of Vacuum Coaters.
7. M. Gahlin, M. Larsson and P. Hedenqvist: 'Me-C:H coatings in motor vehicles', Wear, 2001, 249, 302–209.
8. J. H. Arps, R. A. Page and G. Dearnely: 'Reduction of wear in critical engine components using ion-beam-assisted deposition and ion implantation', Surf. Coat. Technol., 1996, 84, 579–583.
9. Šlechta company website for the DLC coating of the engine's components: https://www.slechta.com/en/services/coating/
10. Delta Faucet company applied DLC coating on the valves. Available online: Delta Faucet Company, US, 2010
11. Example for DLC coating on the kitchen knives blades. Available online: http://nesmuk.de/en/collection/nesmuk-diamor/Dec. 25 2013
12. J. Vetter, 60 years of DLC coatings: Historical highlights and technical review of cathodic arc processes to synthesize various DLC types, and their evolution for industrial applications, Surface and Coatings Technology, Volume 257, 2014, Pages 213-240, ISSN 0257-8972, https://doi.org/10.1016/j.surfcoat.2014.08.017
13. U. Jansson, Erik Lewin, Sputter deposition of transition-metal carbide films — A critical review from a chemical perspective, Thin Solid Films, Volume 536, 2013, Pages 1-24, ISSN 0040 6090, https://doi.org/10.1016/j.tsf.2013.02.019
14. C.A. Love, R.B. Cook, T.J. Harvey, P.A. Dearnley, R.J.K. Wood, Diamond like carbon coatings for potential application in biological implants—a review, Tribology International, Vol. 63, 2013, p. 141-150, ISSN 0301-679X, https://doi.org/10.1016/j.triboint.2012.09.006
15. Jinfeng Cui, Li Qiang, Bin Zhang, Xiao Ling, Tao Yang, Junyan Zhang, Mechanical and tribological properties of Ti-DLC films with different Ti content by magnetron sputtering technique, Applied Surface Science, Volume 258, Issue 12, 2012, Pages 5025-5030, ISSN 0169-4332, https://doi.org/10.1016/j.apsusc.2012.01.072
16. Shi, Feng. (2018). Introductory Chapter: Basic Theory of Magnetron Sputtering. 10.5772/intechopen.80550.

17. Springer-Verlag London 2015. A.Y.C. Nee (ed.), Handbook of Manufacturing Engineering and Technology. DOI 10.1007/978-1-4471-4670-4_28
18. Behrisch R, Bohdansky J, Oetjen GH, Roth J, Schilling G, Verbeek H (1976) J Nucl Mat 60:321
19. Andrew H. Simon, in Handbook of Thin Film Deposition (Third Edition), 2012
20. Wehner GK (1956) Phys Rev 102:690, Wehner GK (1957) Phys Rev 108:35, Wehner GK (1959) Phys Rev 114:1270, Wehner GK (1968) Phys Rev 112:1120.
21. Sigmund P (1974) Appl Phys Lett 25:169
22. Lindhard J, Nielsen V, Scharff M (1968) Mat Fys Medd Dan Vid Selsk 10:36
23. Sigmund P (1968) Can J Phys 46:731
24. Gauri Shanker, P. Prathap, K.M.K. Srivatsa, Preetam Singh, Effect of balanced and unbalanced magnetron sputtering processes on the properties of SnO2 thin films, Current Applied Physics, Issue 6, 2019, Pages 697-703, https://doi.org/10.1016/j.cap.2019.03.016
25. Gennardo, David. (2011). Design, construction, and optimization of a magnetron sputtering system for urania deposition.
26. Liu, Cheng-Tsung & Yeh, Hsiao-Chun & Chung, He-Yu & Hwang, Chang-Chou. (2014). Design Assessments of a Rectangular DC Magnetron Sputter for Extended Target Life and Faster Sputtering. Magnetics, IEEE Transactions on. 50. 1-4. 10.1109/TMAG.2013.2278836
27. Jinlong Jiang, Junying Hao, Xianjuan Pang, Peng Wang, Weimin Liu, Structure and characteristics of amorphous (Ti, Si)–C:H films deposited by reactive magnetron sputtering, Diamond and Related Materials, Issue 10, 2010, Pages 1172-1177, https://doi.org/10.1016/j.diamond.2010.05.005
28. Guojia Ma, Shuili Gong, Guoqiang Lin, Lin Zhang, Gang Sun, A study of structure and properties of Ti-doped DLC film by reactive magnetron sputtering with ion implantation, Applied Surface Science, Issue 7, 2012, Pages 3045-3050, ISSN 0169-4332, https://doi.org/10.1016/j.apsusc.2011.11.034
29. The technical data of the "PPP-NCHAu" cantilever provided by the manufacturer. Available online:https://www.nanosensors.com/pointprobe-plus-non-contact-tapping-mode-high-resonance-frequency-au-coating-detector-side-afm-tip-PPP-NCHAuD
30. Li, C.; Huang, L.; Yuan, J. Effect of sp3 Content on Adhesion and Tribological Properties of Non-Hydrogenated DLC Films. Materials 2020, 13, 1911. https://doi.org/10.3390/ma13081911
31. The technical data of the polymer cantilever provided by the manufacturer Available online: https://www.nanoandmore.com/AFM-Probe-CP-FM-PM
32. Wei Dai, Peiling Ke, Myoung-Woon Moon, Kwang-Ryeol Lee, Aiying Wang, Investigation of the microstructure, mechanical properties and tribological behaviors of Ti-containing diamond-like carbon films fabricated by a hybrid ion beam method, Thin Solid Films, Volume 520, Issue 19, 2012, Pages 6057-6063, ISSN 0040-6090, https://doi.org/10.1016/j.tsf.2012.04.016
33. Jo, Yeong Ju & Zhang, Teng Fei & Son, Myoungjun & Kim, Kwang. (2017). Synthesis and electrochemical properties of Ti-doped DLC films by a hybrid PVD/PECVD process. Applied Surface Science. 433. https://doi.org/10.1016/j.apsusc.2017.10.151
34. Bharathy, P. Vijai and Nataraj, D. and Chu, Paul K. and Wang, Huaiyu and Yang, Q. and Kiran, M.S.R.N. and Silvestre-Albero, J. and Mangalaraj, D. Effect of titanium incorporation on the structural, mechanical and biocompatible properties of DLC thin films prepared by reactive-

biased target ion beam deposition method, Applied Surface Science, Volume 257, 2010, https://doi.org/10.1016/j.apsusc.2010.06.052

35. Cao H, Qi F, Ouyang X, Zhao N, Zhou Y, Li B, Luo W, Liao B, Luo J. Effect of Ti Transition Layer Thickness on the Structure, Mechanical and Adhesion Properties of Ti-DLC Coatings on Aluminum Alloys. Materials. 2018; 11(9):1742. https://doi.org/10.3390/ma11091742
36. Hongshuai Cao, Xue Ye, Hao Li, Fugang Qi, Qing Wang, Xiaoping Ouyang, Nie Zhao, Bin Liao, Microstructure, mechanical and tribological properties of multilayer Ti-DLC thick films on Al alloys by filtered cathodic vacuum arc technology, Materials & Design, Volume 198, 2021, 109320, ISSN 0264-1275, https://doi.org/10.1016/j.matdes.2020.109320
37. Prakasam M, Locs J, Salma-Ancane K, Loca D, Largeteau A, Berzina-Cimdina L. Biodegradable Materials and Metallic Implants-A Review. J Funct Biomater. 2017 Sep 26;8(4):44. doi: 10.3390/jfb8040044. PMID: 28954399; PMCID: PMC5748551.
38. Dowling DP, Kola PV, Donnelly K, Kelly TC, Brumitt K, Lloyd L, et al. Evaluation of diamond-like carbon-coated orthopaedic implants. Diamond and Related Materials 1997; 6:390–3.
39. Thomas Zehnder, Jörg Patscheider, Nanocomposite TiC/a–C:H hard coatings deposited by reactive PVD, Surface and Coatings Technology, Volumes 133–134, 2000, Pages 138-144, ISSN 0257-8972, https://doi.org/10.1016/S0257-8972(00)00888-4.
40. J. Robertson: 'Diamond-like amorphous carbon', Mater. Sci. Eng. R, 2002, 37, (4–6), 129–281.
41. Y. Lifshitz: 'Diamond-like carbon – present status', Diam. Relat. Mater., 1999, 8, (8–9), 1659–1676.
42. C. J. Hwang, and L. A. K. Watt, Physical Review, 1968. Calculation of the Formation Energy of a Schottky Defect in Germanium. 171 (3), 958 - 969 Crossref.
43. S. V. Hainsworth & N. J. Uhure (2007) Diamond like carbon coatings for tribology: production techniques, characterisation methods and applications, International Materials Reviews, 52:3, 153-174, DOI: 10.1179/174328007X160272
44. Andrea Carlo Ferrari, Determination of bonding in diamond-like carbon by Raman spectroscopy, Diamond and Related Materials, Volume 11, Issues 3–6, 2002, Pages 1053-1061, ISSN 0925-9635, https://doi.org/10.1016/S0925-9635(01)00730-0.
45. Alexandre Merlen, Josephus Buijnsters, Cedric Pardanaud. A Guide to and Review of the Use of Multiwavelength Raman Spectroscopy for Characterizing Defective Aromatic Carbon Solids: from Graphene to Amorphous Carbons. Coatings, MDPI, 2017, 7 (10), ⟨10.3390/coatings7100153⟩. ⟨hal-01596681⟩
46. C. Ferrari, J. R., Resonant Raman spectroscopy of disordered, amorphous and diamond like carbon. Physical Review B 2001, 64 (7), 5414-(1-13).
47. Publishing, 2009, Pages 391-426, ISBN 9781845693589, https://doi.org/10.1533/9781845695477.2.391.
48. Otto Schott Institute for Materials Research website, https://www.osim.uni-jena.de/
49. CC-BY-2. 5; Open source Handbook of Nanoscience and Nanotechnology.
50. The super sharp cantilevers specifications of the Nano And More GmbH company. Available online: https://www.nanoandmore.com/Enhanced-Resolution-SuperSharp-AFM-Probes
51. The utilized atomic force microscopy in this work, manufactured by the JPK instruments company. Available online: https://www.nanophys.kth.se/nanolab/afm/jpk/manuf-manuals/handbook-2.2a.pdf

52. The sharp cantilever “ContAl-G” specification. Available online: https://www.budgetsensors.com/contact-mode-afm-probe-aluminum-contal
53. P. Zhang, B.K. Tay, G.Q. Yu, S.P. Lau, Y.Q. Fu, Diam. Relat. Mater. 13 (2004) 459–464.
54. N. Pasaja, S. Sansongsiri, S. Intarasiri, T. Vilaithong, A. Anders, Nucl. Instrum. Methods in Phys. Res. B 259 (2007) 867–870.
55. S. Sansongsiri, A. Anders, B. Yotsombat, Diamond Relat. Mater. 17 (2008) 2080–2083
56. Özoğul, A., Gräf, S., Müller, F.A. et al. Reverse Stick-Slip on a Periodic Wedge-Shaped Micrograting. Tribol Lett 67, 29 (2019). https://doi.org/10.1007/s11249-019-1139-x
57. Behrad Madjdabadi, Benoît Valley, Maurice B. Dusseault, Peter K. Kaiser, Experimental evaluation of a distributed Brillouin sensing system for measuring extensional and shear deformation in rock, Measurement, Volume 77, 2016, Pages 54-66, ISSN 0263-2241, https://doi.org/10.1016/j.measurement.2015.08.040.
58. B.K. Tay, P. Zhang, Thin Solid Films 420–421 (2002) 177–184
59. Trusovas, Romualdas & Raciukaitis, Gediminas & Niaura, Gediminas & Barkauskas, Jurgis & Pauliukaite, Rasa. (2015). Recent Advances in Laser Utilization in the Chemical Modification of Graphene Oxide and Its Applications. Advanced Optical Materials. 4. n/a-n/a. 10.1002/adom.201500469.
60. B N J Persson et al 2004 J. Phys.: Condens. Matter 17 R1.
61. The Gwyddion software’ user guide. Available online: http://gwyddion.net/documentation/user-guide-en/statistical-analysis.html.
62. Bhushan B. (2007) Nanotribology, Nanomechanics and Materials Characterization. In: Bhushan B. (eds) Springer Handbook of Nanotechnology. Springer Handbooks. Springer, Berlin, Heidelberg. Page 988-989. https://doi.org/10.1007/978-3-540-29857-1_29
63. J. Robertson, Diamond-like amorphous carbon, Materials Science and Engineering: R: Reports, Volume 37, Issues 4–6, 2002, Pages 129-281, ISSN 0927-796X, https://doi.org/10.1016/S0927-796X(02)00005-0.
64. Dariya Savchenko, Vladimir Vorlíček, Andrey Prokhorov, Ekaterina Kalabukhova, Jan Lančok, Miroslav Jelínek, Raman and EPR spectroscopic studies of chromium-doped diamond-like carbon films, Diamond and Related Materials, Volume 83, 2018, Pages 30-37, ISSN 0925-9635, https://doi.org/10.1016/j.diamond.2018.01.021.
65. Wei Dai, Guosong Wu, Aiying Wang, Preparation, characterization and properties of Cr-incorporated DLC films on magnesium alloy, Diamond and Related Materials, Volume 19, Issue 10, 2010, Pages 1307-1315, ISSN 0925-9635, https://doi.org/10.1016/j.diamond.2010.06.018
66. W. Dai, H. Zheng, G. Wu, A. Wang, Effect of bias voltage on growth property of Cr-DLC film prepared by linear ion beam deposition technique, Vacuum. 85 (2010) 231–235. https://doi.org/10.1016/j.vacuum.2010.06.001
67. P. Safaie, A. Eshaghi, S.R. Bakhshi, Oxygen doping effect on the wettability of diamond-like carbon thin films, J. Non. Cryst. Solids. 471 (2017) 410–414. https://doi.org/10.1016/j.jnoncrysol.2017.06.034
68. Marius Černauskas, Liutauras Marcinauskas, Roberts Zabels, Synthesis of nanostructured amorphous carbon-copper composite films by plasma-enhanced chemical vapour deposition, Thin Solid Films, Volume 615, 2016, Pages 195-201, ISSN 0040-6090, https://doi.org/10.1016/j.tsf.2016.07.003.

69. J.A. Santiago, I. Fernández-Martínez, J.C. Sánchez-López, T.C. Rojas, A. Wennberg, V. Bellido-González, J.M. Molina-Aldareguia, M.A. Monclús, R. González-Arrabal, Tribomechanical properties of hard Cr-doped DLC coatings deposited by low-frequency HiPIMS, Surface and Coatings Technology, Volume 382, 2020, 124899, ISSN 0257-8972, https://doi.org/10.1016/j.surfcoat.2019.124899
70. S. Zhang, M. Yan, Y. Yang, Y. Zhang, F. Yan, H. Li, Excellent mechanical, tribological and anti-corrosive performance of novel Ti-DLC nanocomposite thin films prepared via magnetron sputtering method, Carbon N. Y. 151 (2019) 136–147. doi: 10.1016/j.carbon.2019.05.031.
71. N.W. Khun, E. Liu, G.C. Yang, Structure, scratch resistance and corrosion performance of nickel doped diamond-like carbon thin films, Surf. Coatings Technol. 204 (2010) 3125–3130. doi: 10.1016/j.surfcoat.2010.02.057.
72. L. Sun, X. Zuo, P. Guo, X. Li, P. Ke, A. Wang, Role of deposition temperature on the mechanical and tribological properties of Cu and Cr co-doped diamond-like carbon films, Thin Solid Films. 678 (2019) 16–25. doi: 10.1016/j.tsf.2019.03.034.
73. B. Zhou, Z. Liu, D.G. Piliptsou, S. Yu, Z. Wang, A. V. Rogachev, A.S. Rudenkov, A. Balmakou, Structure and optical properties of Cu-DLC composite films deposited by cathode arc with double-excitation source, Diam. Relat. Mater. 69 (2016) 191–197. doi: 10.1016/j.diamond.2016.09.004.
74. B. Pandey, S. Hussain, Effect of nickel incorporation on the optical properties of diamond-like carbon (DLC) matrix, J. Phys. Chem. Solids. 72 (2011) 1111–1116. doi: 10.1016/j.jpcs.2011.06.003.
75. A.M. Qasim, Q. Ruan, R.K.Y. Fu, F. Ali, B. Mehrjou, H. Wu, L. Liu, Z. Wu, P.K. Chu, Enhanced oxygen-induced properties of bulk oxygenated amorphous carbon films deposited with an anode layer ion source, Vacuum. 169 (2019) 108915. doi: 10.1016/j.vacuum.2019.108915.
76. M. Evaristo, R. Azevedo, C. Palacio, A. Cavaleiro, Influence of the silicon and oxygen content on the properties of non-hydrogenated amorphous carbon coatings, Diam. Relat. Mater. 70 (2016) 201–210.
77. Paul E. West, Introduction to Atomic Force Microscopy, Theory, Practice, Applications. P. 7-8. Julius Maximilians University of Würzburg.

Appendices

Appendix 1. JPK software

In **Fig. 40** the info window can be seen, it provides the whole measurement parameters which were used during the measurement. As well in **Fig. 41** the home window of the JPK software can be seen. It allows the user to control and monitor the measurement operation.

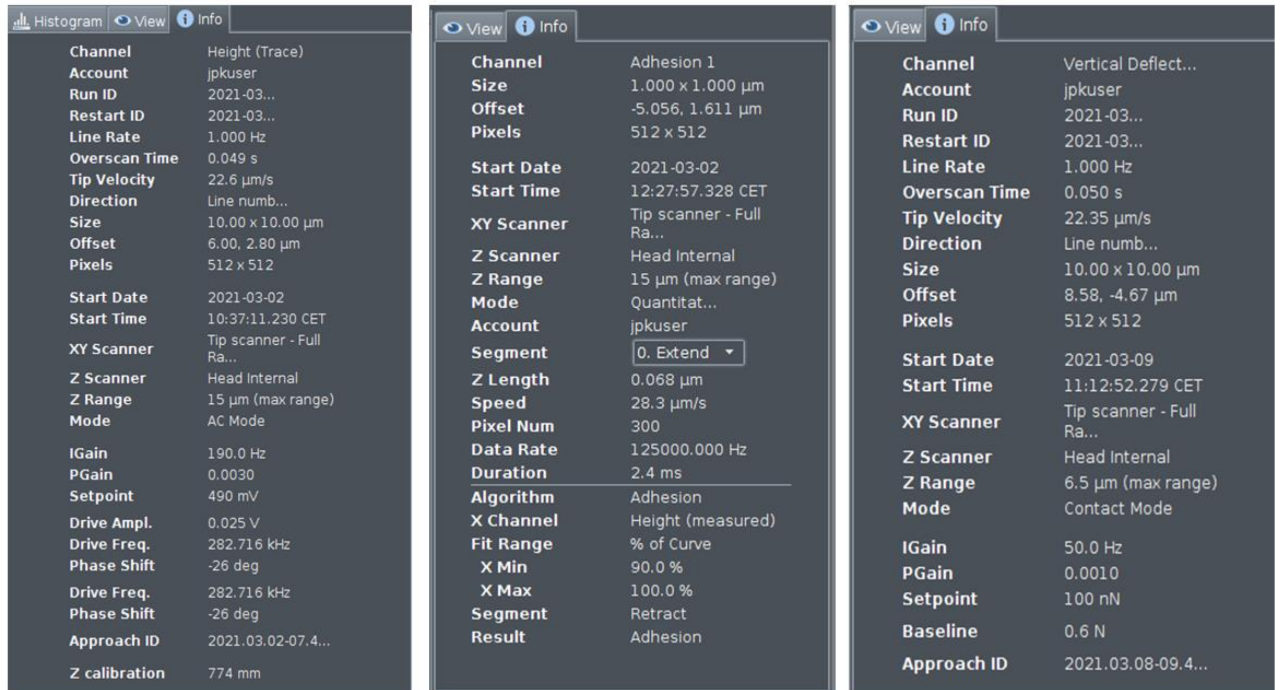

Fig. 40. The measurement parameters, as seen from the JPK software, of the sample Ti-DLC3 from right to left, roughness, adhesion and friction.

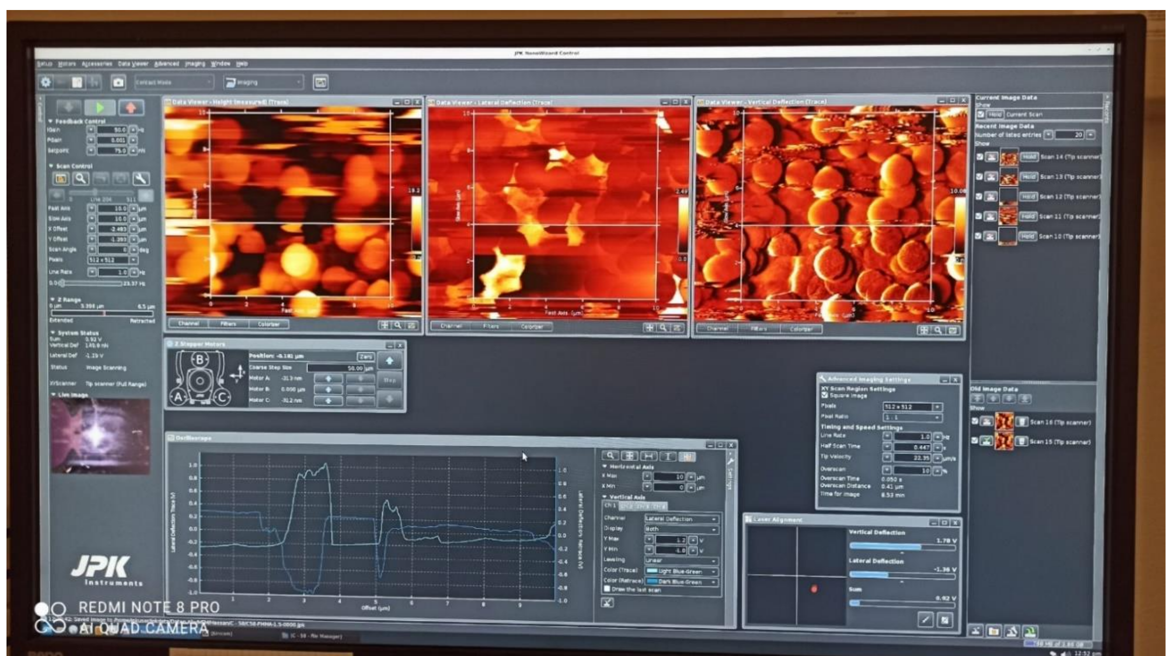

Fig. 41. The home window of the JPK software used to monitor and control the measurement process.

Appendix 2. Gwyddion software

In **Fig. 42** the main window of the Gwyddion software is shown. As well the Gwyddion user guide main page. This software was used in the data processing of the images results from AFM. As well this software provides extremely wide types of tools and functions.

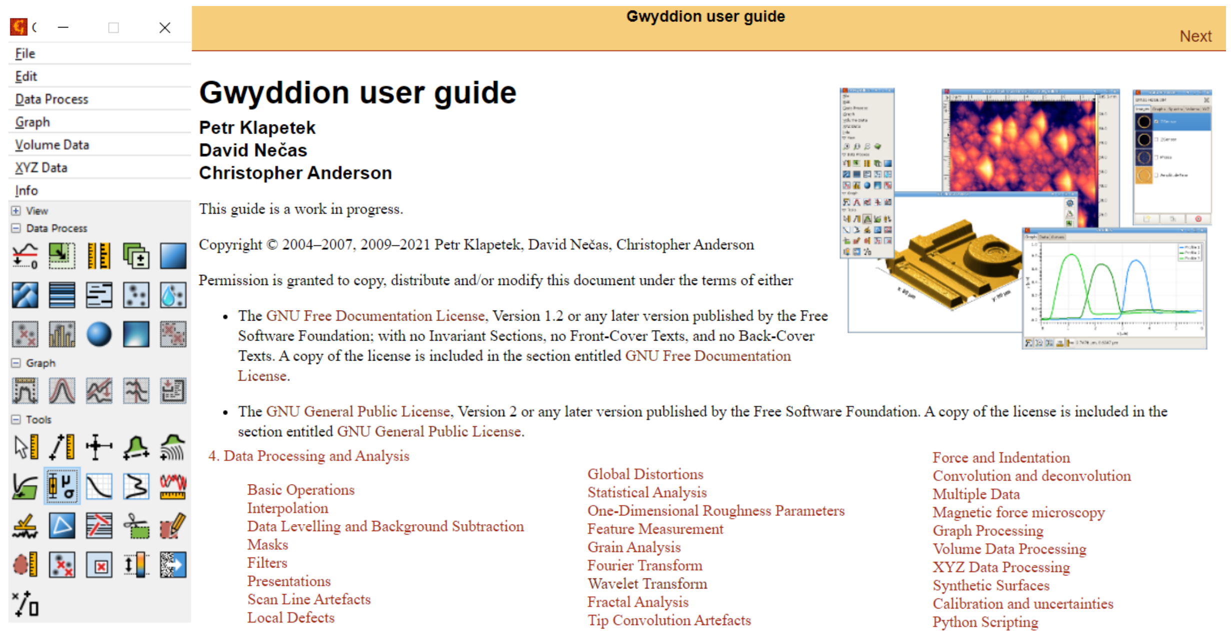

Fig. 42. The Gwyddion main and user guide windows [61].